Climate Dynamics (2002) 19: 43–60
DOI 10.1007/s00382-001-0208-6

M. Crucifix · M.-F. Loutre · P. Tulkens
T. Fichefet · A. Berger

Climate evolution during the Holocene: a study with an Earth system model of intermediate complexity

Received: 12 February 2001 / Accepted: 1 October 2001 / Published online: 12 January 2002

Abstract An Earth system model of intermediate complexity, MoBidiC, has been used to simulate the transient variations in continental temperature, sea-surface temperature (SST), thermohaline circulation (THC) and sea-ice cover over the last 9000 years (9 kyr). Experiments were designed to determine (a) the deviation of the climatic system with respect to equilibrium over the last 9 kyr, (b) the individual contributions of oceans and vegetation to climatic changes, as well as the potential synergies between these components, and (c) the relative importance of precession, obliquity and CO_2 concentration changes during this period. Results show a monotonous cooling trend in the northern high latitudes between 9 kyr BP and the present day, both over the oceans and the continents. North of 60°N, this cooling is noticed throughout the year, but the largest variations appear in spring and summer (up to 6 °C over continents). Along with this cooling, the model exhibits a southward shift of the northern treeline by about 600 km. Most of this shift takes place between 4 and 1 kyr BP. During this period, reorganisations of the boreal forest introduce a lag of about 200 years in the system with respect to a state in equilibrium with the external forcing. Sensitivity experiments illustrate the strong impact of this vegetation shift both on the oceans and the continents, especially in spring and early summer. However, the model exhibits a weak synergy between vegetation and ocean throughout the Holocene. Finally, a sensitivity study to the forcing components shows the dominant role of the astronomical forcing with respect to CO_2, as well as the non-linear behaviour of climate in response to obliquity and precession.

M. Crucifix (✉) · M.-F. Loutre · P. Tulkens
T. Fichefet · A. Berger
Institut d'Astronomie et de Géophysique G. Lemaître,
Université catholique de Louvain, 2 Chemin du Cyclotron,
B-1348 Louvain-la-Neuve, Belgium
E-mail: crucifix@astr.ucl.ac.be

1 Introduction

The Holocene (taken here as the last 9000 years) appears in the polar records as a period of relative stability when compared to glacial ages. However, important changes occurred in paleoenvironmental conditions in the northern mid- and high latitudes as well as in the tropics.

In Europe, for example, paleobotanic reconstructions suggest that the surface temperature went through a maximum about 6000 years ago with, in particular, milder winters than today in Scandinavia (Huntley and Prentice 1988). Similarly, foraminifera- and diatom-based reconstructions (Ruddiman and Mix 1993; Koç et al. 1993; Kerwin et al. 1999) reveal that the SST in the northern North Atlantic was higher than today during the early Holocene, with a deviation in summer that could have been as high as 4 °C. In the tropical areas, changes are essentially seen in precipitation, the Asian and African monsoons being more intense and shifted northwards between 9 and 5 kyr BP as compared to today (Street-Perrott et al. 1990; Gasse 2000).

Since the pioneering modelling study of the Holocene climate by Kutzbach and Otto-Bliesner (1982), there has been a general consensus to consider the astronomical forcing as the fundamental cause of these variations. Indeed, at 9 kyr BP, the Earth reached the perihelion during the northern summer, while today it occurs in winter. This effect can be quantified by the change in the precession parameter (eccentricity times the sine of the longitude of the perihelion) that increased from –0.0145 (Northern Hemisphere summer solstice at perihelion) to 0.0164 (Northern Hemisphere summer solstice at aphelion) over this period (Fig. 1a) (Berger 1978). The consequence for the Northern Hemisphere is a gradual weakening of the amplitude of the seasonal cycle of insolation at the top of the atmosphere, resulting in a decrease in the hemispheric average of June insolation by 33 W/m^2 (6%) to the benefit of the January insolation. In addition to precession, obliquity (i.e. the tilt of

the Earth's rotational axis) decreased by about 1° over the last 9 kyr BP (Fig. 1b). Such a decrease in obliquity causes a decrease of insolation in the summer hemisphere. Hence, in the Northern Hemisphere, the effects of precession and obliquity on June insolation summed up during the Holocene. For example, at 65°N, the summer solstice insolation decreased by about 46 W/m^2 (10%) between 9 kyr BP and today (Fig. 1c). In addition to its effect on summer insolation, the decrease in obliquity caused an increase in annual mean insolation between 43°S and 43°N at the expense of the high latitudes. Namely, annual mean insolation at 65°N decreased by 2.5 W/m^2 (slightly more than 1%) between 9 kyr BP and today (Fig. 1d).

In order to test to which extent the astronomical forcing could explain the observed climatic changes, a large number of model studies have been performed. The first ones were based on atmospheric general circulation models (AGCMs) (Kutzbach and Otto-Bliesner 1982; Kutzbach et al. 1993; Hall and Valdes 1997; Joussaume and Braconnot 1997; Joussaume et al. 1999). These model studies pinpointed the main consequences of the changes in the seasonal and spatial distributions of insolation between the mid-Holocene and today, i.e. for 6 kyr BP, warmer summers in the Northern Hemisphere and intensified northern tropical monsoon due to enhanced sea-land temperature contrast. However, they did not succeed in reproducing correctly the amplitude of the climatic changes as recorded in data. For example, in the Sahara, the precipitation increase between the mid-Holocene and today simulated by these AGCMs was too small to allow vegetation to develop in this area as suggested by paleoenvironmental records. This is most likely because important potential sources of feedbacks, such as vegetation and ocean, were not taken into account. In this context, a growing effort has been devoted to assess the impact of vegetation changes in AGCMs. Foley et al. (1994) showed, for example, that in AGCM simulations of the 6 kyr BP climate, prescribing a more northward extension of taiga (cold boreal forest) caused, at northern high latitudes, an additional warming of 4 °C in spring and 1 °C in the other seasons. Likewise, Kutzbach et al. (1996) noticed that replacing desert with grassland in North Africa further enhances summer precipitation by 12% in this area. TEMPO (1996) and Harrison et al. (1998) adopted the inverse approach by showing that, when using the climate simulated at 6 kyr BP by various AGCMs, the BIOME vegetation model predicts an expansion of boreal forest to 1.20 times of its modern area as well as an expansion of 'moisture-demanding' vegetation in the African and Asian subtropics. As a step beyond, several coupled vegetation-atmosphere models have been developed and utilised to study the mid-Holocene climate. Claussen and Gayler (1997) simulated, with the ECHAM-BIOME model, an increase by 300% in summer precipitation in North Africa, along with a 6° northward advance of savanna in the western Sahara, which suggest that the climate changes in response to the astronomical forcing are even larger when the positive feedbacks between climate and vegetation are taken into account. This result was subsequently corroborated by Texier et al. (1997) and Doherty et al. (2000) (with, however, a less dramatic increase in North African precipitation). Texier et al. (1997) also reported a reduction of boreal tundra area by 25%.

In parallel, simulations of the mid-Holocene climate with coupled atmosphere–ocean models (AOGCMs) highlighted the positive feedback of the ocean for the penetration of northern summer monsoon (Kutzbach and Liu 1997; Hewitt and Mitchell 1998; Bush 1999; Braconnot et al. 2000). Otto-Bliesner (1999) also stressed the possible role played by changes in ENSO regimes for Sahel precipitation. Very recently, AOGCM simulations with an interactive vegetation component started to be conducted: Braconnot et al. (1999) found that the positive feedbacks of vegetation and ocean for summer monsoon do not merely sum up but exhibit a positive

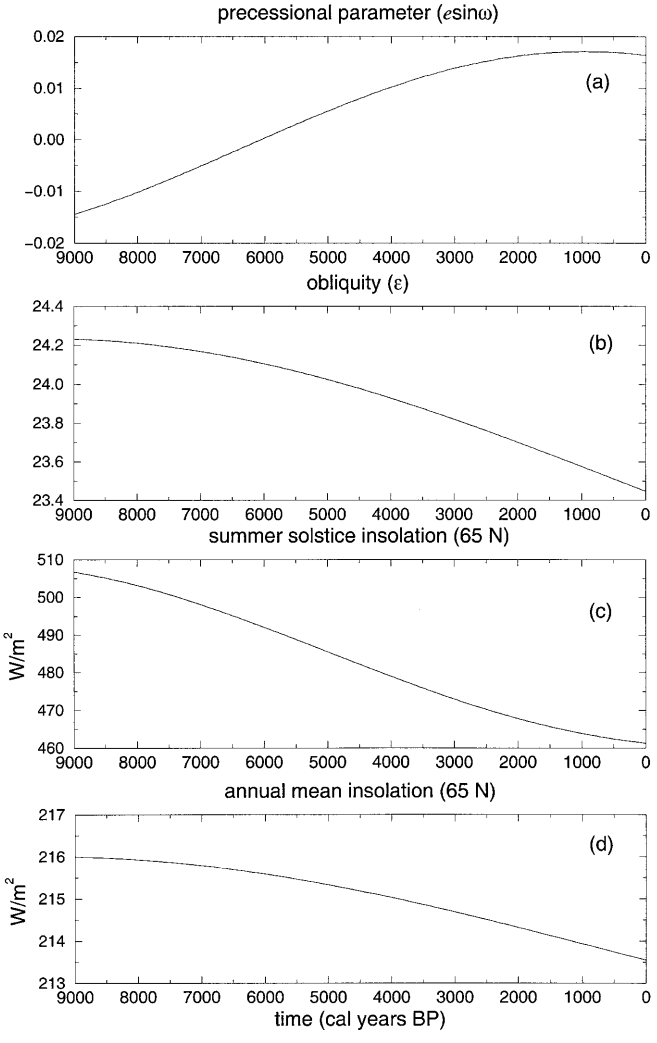

Fig. 1a–d Astronomical forcing over the last 9 kyr BP. **a** Precession parameter, defined as eccentricity times the sine of the perihelion; **b** obliquity; **c** summer solstice insolation at 65°N; **d** Annual mean insolation at 65°N

synergy. Up to now, no ocean-vegetation-GCM study focused on ocean-vegetation synergies in the northern high latitudes.

Despite the increasing performance of these GCMs, their results remain difficult to interpret. First, GCM simulations assume that the climate is in equilibrium with the external forcing, which is not necessarily the case. Secondly, they do not give information about the time evolution of the system, and, in particular, about the timing of the important climatic transitions. Finally, the high computational cost of these models makes it impossible, in practice, to afford a large number of sensitivity tests. A complementary approach, based on Earth system models of intermediate complexity, is followed here to overcome these problems. These models have a coarse resolution and include physical processes with a higher level of parametrisation. However, they include a large number of climatic components (this is sometimes referred to as *integration*) and their advantageous computing cost allows for numerous transient experiments over several millennia (Claussen et al. 2001).

Ganopolski et al. (1998) initiated this approach for the Holocene. They used an Earth system model of intermediate complexity to study the feedbacks and synergies related to ocean and vegetation in the 6 kyr BP climate. The same model was then used to study the transient behaviour of climate throughout the last 9 kyr (Claussen et al. 1999). The authors suggested, in particular, that the abrupt desertification of the Sahara, some 5000 years ago, is a response to the astronomical forcing amplified by a positive feedback between vegetation and precipitation. The present study is in the line of this approach, but with a focus on the northern high latitudes. At these latitudes, vegetation is not so much limited by precipitation but rather by summer temperature (Woodward 1987; Prentice et al. 1992). Hence, as an extension of the work by Claussen et al. (1999) about the vegetation-precipitation feedback in the tropics, we will try to determine whether the vegetation-temperature feedback in the high latitudes could have triggered rapid shifts of the northern treeline position in response to the astronomical forcing. According to data, such a rapid displacement of the treeline possibly occurred between 4000 and 1000 years ago (MacDonald et al. 2000).

To reach this goal, we have investigated the time-dependent response of the climatic system to insolation and CO_2 variations during the Holocene using MoBidiC. This climate model includes dynamical equations for the atmosphere, the oceans, the sea ice, the land surface and the terrestrial vegetation. We proceeded in two steps. First, two snapshot experiments were performed in order to compare the model performance against present-day climatology and outputs from GCMs for the 6 kyr BP climate, respectively (Sect. 3). Next, a series of nine transient experiments over the last 9 kyr have been carried out (Sect. 4). These transient experiments were designed (1) to examine the respective roles played by changes in vegetation, ocean temperature and sea-ice area during the Holocene, and (2) to discriminate between the impacts of precession, obliquity and atmospheric CO_2 concentration. Discussion and conclusion follow in Sect. 5.

2 Description of model and calendar

2.1 Model

MoBidiC is described in the Appendix. Here, we only give the main elements relevant for the discussion of the results. The model links a zonally averaged atmospheric model to sectorial representations of the land surface and of the ocean. This means that each zonal band is divided into different sectors representing the main continents (Eurasia-Africa and America) and oceans (Atlantic, Pacific and Indian). Each continental sector can be partly covered by snow, and similarly, each oceanic sector can be partly covered by sea ice (with a possible snow layer). The atmospheric component is based on the zonally averaged, quasi-geostrophic formalism and includes additional parametrisations to represent the transports by the Hadley cells. This quasi-geostrophic atmospheric model is much more efficient than the primitive-equation formalism because it allows for a rather large time step (two days, here). The relatively high number of parameters in the Hadley cell parametrisation requires, however, a careful assessment of the model's sensitivity to these internal parameters (Gallée et al. 1991). The radiative transfer explicitly calculates the downward and upward longwave and shortwave radiations in up to 15 vertical layers. The ocean component is based on the sectorially averaged form of the multilevel, primitive-equation ocean model of Bryan (1969). A simple thermodynamic–dynamic sea-ice component is coupled to the ocean model. It is based on the zero-layer thermodynamic model of Semtner (1976), but includes an advection scheme with prescribed ice velocities. Finally, MoBidiC includes the dynamical vegetation model VECODE developed by Brovkin et al. (1997). It is based on a continuous bioclimatic classification which describes vegetation as a composition of simple plant functional types (trees and grass). Equilibrium tree and grass fractions are parametrized as a function of climate expressed as a sum of degree-days and annual precipitation.

2.2 Calendar

Discussion of paleoclimate simulations requires an accurate definition of the calendar used, i.e. how months and seasons are defined. In MoBidiC, each year is divided into 12 months of 30 days each. The vernal equinox is the 80th day of the year. Another possibility would have been to define months of equal Sun true longitude interval. Both calendars present the advantage to avoid as much as possible references to the present-day Gregorian calendar, except for the choice of the vernal equinox. During the Holocene, the first day of a given month may differ by up to five days depending on the selected definition (equal longitude or duration). Although Joussaume and Braconnot (1997) suggested that a month definition based on its angular length may be more appropriate for comparing model outputs with paleorecords because this "*better accounts for the phasing of the insolation curves*", we preferred to keep month of equal duration as a more convenient way to present the seasonal evolution of temperature and sea-ice area. However, summer and winter temperatures will generally be represented by the maximum and minimum values of the seasonal cycle, which do not depend on the calendar.

3 Snapshot experiments

3.1 Control experiment: pre-industrial forcing

The control simulation is performed with present-day insolation and a CO_2 concentration of 280 ppmv. The equilibrium is

obtained by starting the model integration from present-day climatological conditions for the atmospheric component, and oceanic temperature and salinity distributions simulated with the ocean-alone model using a surface restoring to present-day temperature and salinity fields (Hovine and Fichefet 1994). The model, including the dynamical vegetation scheme, then evolves towards its own equilibrium. After 15,000 years of integration, the simulated climate is stable, with a global annual mean surface temperature of 14.5 °C and a global annual mean SST of 18.0 °C. The seasonal cycle of the zonally averaged surface temperature compares favourably with Kalnay et al's (1996) data, although some discrepancies are noticed (Fig. 2). First, the model exhibits a cold bias in the northern polar regions, mainly in winter. This bias is caused by the absence of deep convection in the Atlantic basin north of 60°N and by the fact that the northward advection of warm water along the Norwegian coast up to 75°N is not accounted for. In addition, there is a warm deviation reaching 4 °C in the 30–50°N latitude band. The model also slightly overestimates the surface temperature in equatorial regions, especially during the first half of the year.

The model captures the main features of the annual mean SSTs and sea-surface salinities (SSSs) as observed by Levitus (1982) (Fig. 3). However, SSTs are generally too cold near the equator and too warm in the tropics, especially in the Pacific Ocean. Besides, the model does not reproduce well the salinity maxima observed in the tropics. In the North Pacific, simulated SSS appears overestimated, which artificially induces water sinking down to about 750 m.

Figure 4 shows that the modelled deep-ocean temperatures are in qualitative agreement with observations. The warm water pool simulated at depth in the northern polar regions is attributed to the lack of convection north of 60°N in the Atlantic, as discussed already. The figure also reveals the model limitation in simulating the ocean dynamics in equatorial regions, the thermocline being shifted downwards with respect to observations there. The modelled southward transport of North Atlantic Deep Water (NADW) at 27.5°S amounts to 12.4 Sv (1 Sv = $10^6 m^3/s$) (not shown), and Antarctic Bottom Water (AABW) recirculates below NADW up to 30°N in the North Atlantic, in agreement with the description of water-mass distribution in the global ocean given by Schmitz (1995).

The annual mean meridional oceanic heat transport, taken positive northwards, amounts to 1.75 PW at 20°N and to –1.52 PW at 25°S, which is consistent with observational estimates (e.g. Hsiung 1985; Trenberth and Solomon 1994). The simulated total ocean–atmosphere meridional heat transport (Fig. 5) also favourably compares with observations (e.g. Keith 1995). However, in the atmosphere, the model overestimates the dry static heat transport at the expense of the latent heat transport, the latter being too weak, especially in the intertropics. Although the formalism of the atmospheric model would make it possible to remedy this shortcoming by an appropriate parameter adjustment, such an operation would degrade the performance of the oceanic model because this zonally averaged model is not able to transport a large enough amount of salt from the equator to the mid-latitudes, mainly because the horizontal gyres are not represented. Therefore, the underestimation of the atmosphere latent heat transport should rather be viewed as a limitation inherent to the structure of the oceanic model than one of the atmospheric component.

Finally, the observed seasonal cycle of the Arctic sea-ice cover is satisfactorily reproduced, the model predicting a maximum ice area of 14.7×10^6 km^2 in March and a minimum of 6.4×10^6 km^2 in September. This is in broad agreement with the values of 12.2 and 6.0×10^6 km^2 reported from the satellite observations analysis by Gloersen et al. (1992). In the Southern Ocean, the modelled ice pack disappears almost completely in summer, with an area of about 0.5×10^6 km^2 in March. It forms during the winter season, and its maximum area amounts to 11.8×10^6 km^2 in September, which is slightly underestimated when compared to the 14×10^6 km^2 reported by Gloersen et al. (1992).

3.2 Six kyr BP snapshot experiment

The 6 kyr BP climate has been extensively studied, in particular in the framework of the Global Palaeovegetation Mapping project (BIOME 6000, Prentice and Webb 1998) and in the Paleoclimate modelling intercomparison project (PMIP, Joussaume et al. 1999). Hence, before discussing transient simulations, it was relevant to perform a simulation of the 6 kyr BP climate with MoBidiC in order assess its sensitivity and to confront it with these earlier published model results and data.

The model is started from its pre-industrial equilibrium and is run under 6 kyr BP orbital forcing (Berger 1978) (Fig. 6a) and a CO_2 concentration of 267 ppmv (Indermühle et al. 1999) over 15,000 years. The Greenland and Antarctic ice sheets are prescribed as today.

3.2.1 Continental surface temperature

The seasonal and latitudinal distribution of the 6 kyr BP –0 kyr difference in insolation at the top-of-the-atmosphere and in simulated continental temperatures are compared in Fig. 6a,b. North of 60°N, the model simulates a warming throughout the year, of about 4 °C in spring and summer and 1 °C in autumn and winter. The southward displacement of the northern treeline plays an important

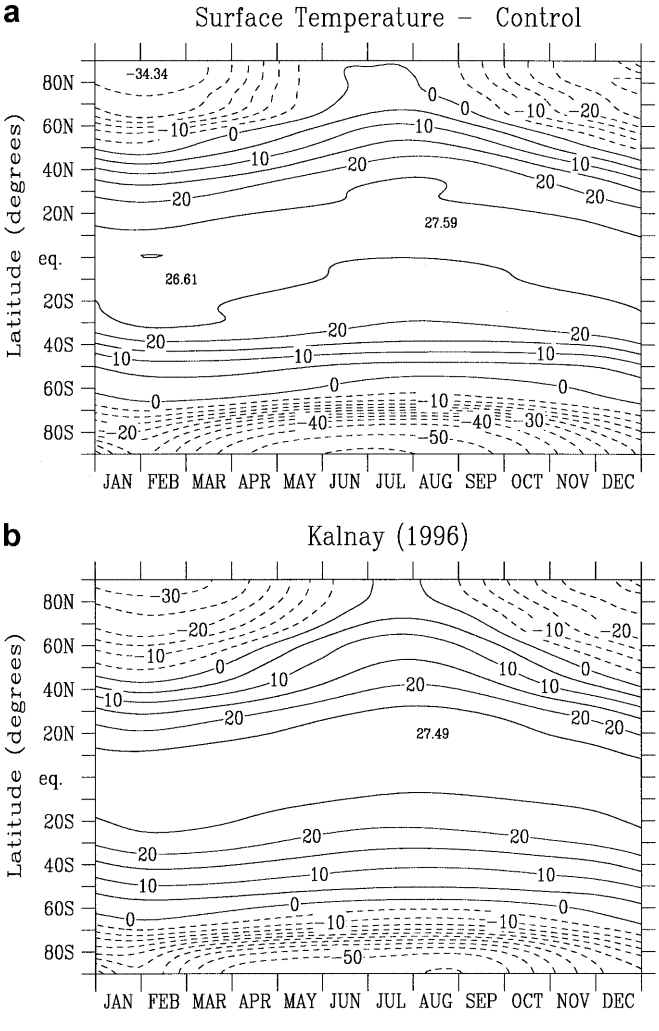

Fig. 2a, b Seasonal cycle of zonally averaged surface temperature (in °C) as a function of latitude. **a** Control simulation results are compared to **b** observations by Kalnay (1996)

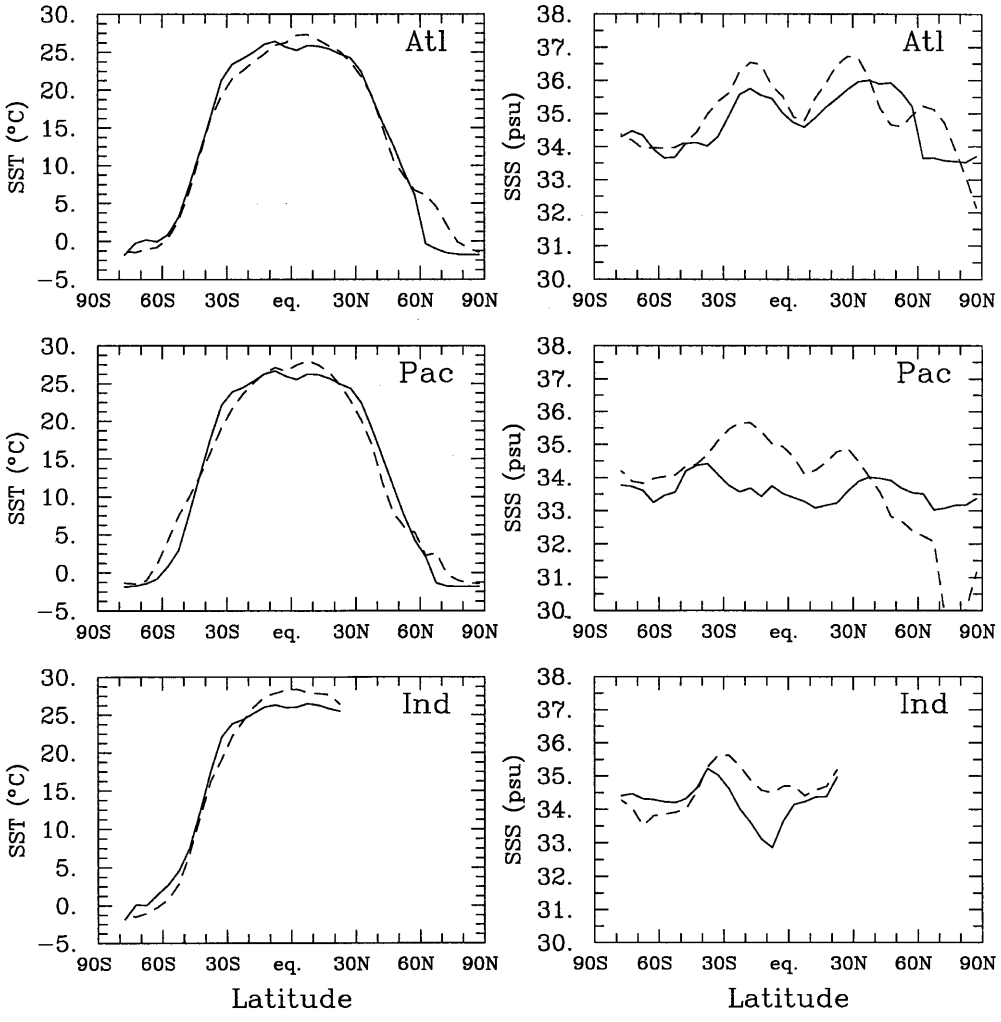

Fig. 3 Latitudinal distributions of the annual mean, zonally averaged SST (*left-hand side*, in °C) and sea-surface salinity (*right-hand side*, in psu) over the three ocean basins. Control simulation results (*solid line*) are compared to Levitus' (1982) observations (*dashed line*)

role on this warming, by contributing about 5 °C of the temperature increase during spring and about 1 °C during summer (Sect. 3.2.5). This is consistent with both models and data (Foley et al. 1994; Texier et al. 1997; Prentice and Webb 1998), although a warming as high as 5 °C is in the upper range of usual estimates.

South of 60°N, vegetation changes are smaller and have much less impact on climate than in the high latitudes. Hence, surface continental temperatures reproduce roughly the insolation anomalies with a lag by about 1 month due to the continental thermal inertia. As a consequence of the tilt of the insolation anomaly pattern shown in Fig. 6a, the maximum temperature deviation occurs later in the year as one moves southward. This tilt also appears when using a calendar based on true longitude intervals, so that one can say that the tilt of the temperature pattern is not qualitatively affected by the choice of calendar (Berger 1983; Joussaume and Braconnot 1997). The main disagreement between MoBidiC and GCMs concerns the tropics. Indeed, an AGCM (Hall and Valdes 1997) and an AOGCM (Braconnot et al. 2000) simulate colder summers than at present in the northern tropical regions (especially in Africa). In the GCMs, monsoon intensification and the associated increase in continental precipitation produce an increase in both soil moisture and wind speed. Both features enhance continental evaporation, eventually cooling the surface.

3.2.2 Sea-surface temperature

The SST deviation pattern mimics the insolation pattern with a time lag of about 75 days (Fig. 6c). Because of the ocean thermal inertia, the lag is larger than on the continent and temperature deviations are reduced in magnitude. The Northern Hemisphere maximum deviation occurs in September–October, between 30 and 70°N. Interestingly, the deviation is slightly weaker in the 50–60°N band because the winter mixed layer is very deep there (up to 1500 m in the Atlantic). This induces a very high thermal inertia, so that the amount of heat necessary to increase the SST in spring and summer is larger than in the neighbouring latitudes. This feature is also present in the GCM results of Braconnot et al. (2000). As noticed for continental temperatures, the maximum deviation occurs later as one moves southwards, reflecting the pattern of insolation deviations. As a consequence, the summer meridional SST gradient in the Northern Hemisphere is slightly reduced when compared to today, August temperatures experiencing the largest positive variations in the highest latitudes. For the following discussion, it is worth stressing that the magnitudes of the SST deviations simulated here are compatible with previous estimates based on OAGCMs using explicit ocean dynamics (Hewitt and Mitchell 1998; Otto-Bliesner 1999; Braconnot et al. 2000).

3.2.3 Heat transport

The pattern of the atmospheric heat-transport changes (Fig. 7a) is essentially characterised by a decrease of summer atmospheric transport by about 0.5 PW, centred between 0 and 40°N. This difference shows the response of the Hadley cells to the smaller meridional gradient of insolation in summer and is consistent with the AOGCM results presented by Braconnot et al. (2000). Contrary to the atmosphere, the oceanic transport is very little affected (Fig. 7b). Changes do not exceed 0.1 PW, which is too small to

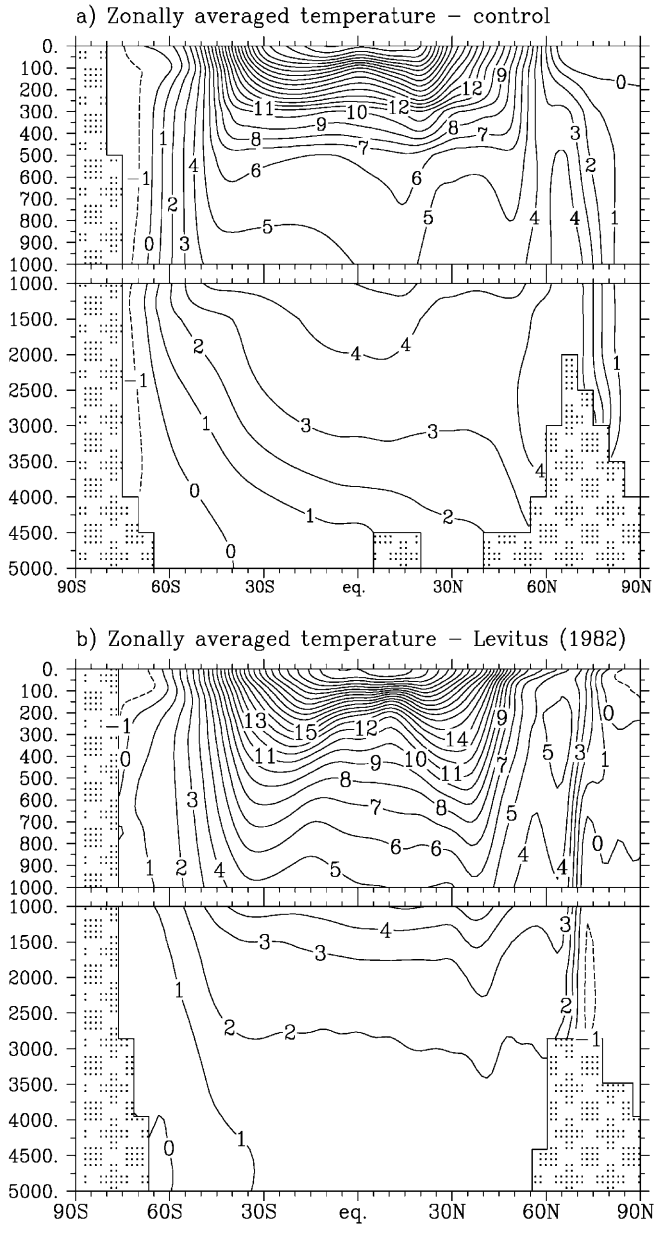

Fig. 4a, b Latitude-depth distributions of the annual mean, zonally averaged potential temperature (in °C) in the global ocean. **a** Control simulation results; **b** observations of Levitus (1982)

produce a significant variation in the heat balance. In particular, the simulated thermohaline circulation is almost identical at 6 kyr and 0 kyr BP, NADW being exported in both cases at a rate of 12.4 Sv at 27.5°S.

3.2.4 Arctic sea ice

Figure 8 displays the seasonal cycles of the simulated Arctic sea-ice area for 6 kyr BP and 0 kyr BP. At 6 kyr BP, larger spring and summer insolation accelerates the summer sea-ice melting, reducing by 3×10^6 km^2 (i.e. 40%) the area of the perennial ice pack. In annual mean, the Arctic sea-ice area is reduced by 9% with respect to today. This decrease is much weaker than the one obtained by Ganopolski et al. (1998), the main difference being that, in the present study, no change occurs in winter sea-ice. Unfortunately,

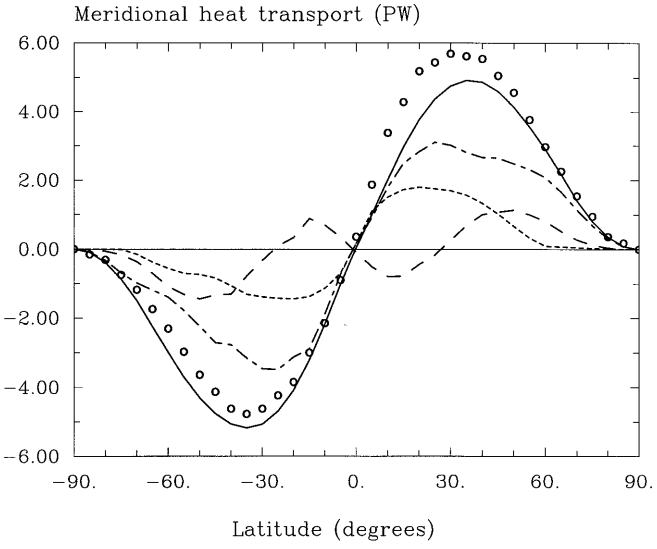

Fig. 5 Modelled annual mean total northward heat transport (*solid line*) with the different contributions: atmospheric dry static transport (*dot-dashed*), atmospheric latent heat transport (*dashed*) and oceanic transport (*dotted*). The *circles* represent the total heat transport of energy in the atmosphere–ocean system estimated by Keith et al. (1995)

data do not enable us to be conclusive. Qualitative reconstructions based on driftwood and whale bones (Kerwin et al. 1999 and references herein) as well as the more quantitative estimates based on dinocysts assemblages by de Vernal and Hilaire-Marcel (2000) support the fact that the summer Arctic sea ice was less extensive during the mid-Holocene with respect to today, but they do not give clear indications about its winter areal coverage.

3.2.5 Vegetation

The 6 kyr climate is characterised by a northward displacement of the boreal treeline with respect to today (Fig. 9). This treeline shift is essentially due to a warmer and longer growing season at 6 kyr. Indeed, the model represents the impact of summer temperature on vegetation by the way of the GDD0 index (growing degree-days above 0 °C) that is defined as the annual sum of the continental surface air temperatures for days during which this temperature exceeds 0 °C (this is the growing season). In this way, both summer temperature and the length of the growing season (i.e. number of days of positive temperature) are taken into account. In MoBidiC, the larger summer insolation in June produces an initial northward displacement of the treeline (i.e. an extension of taiga). As a consequence, snow albedo is reduced. This accelerates the snow melting in spring and early summer, so that positive temperatures appear earlier in the seasonal cycle. This lengthens the growing season and strengthens the vegetation shift. The combination of warmer summers (by up to 4 °C between 60 and 70°N between 6 kyr BP and present) and longer growing seasons (by 18 days between 6 kyr BP and present) eventually increases the GDD0 index (zonally averaged between 60 and 70 °C) by 75%, resulting in a northward treeline shift of 600 km. Such a shift is larger than usually estimated (Prentice and Webb 1998; MacDonald et al. 2000), which may suggest a tendency of the model to overestimate the impact of the astronomical forcing on the treeline position. Comparisons with vegetation-GCM coupled models lead us to similar conclusions: the simulated 6 kyr BP boreal forest expands here to 1.31 times its modern area (19.6×10^6 km^2 instead of 15.0×10^6 km^2), while according to GCM-based predictions, this expansion should not exceed 1.20 (Harrison et al. 1998). A possible explanation of this too strong sensitivity might be the lack of convection sites in the ocean

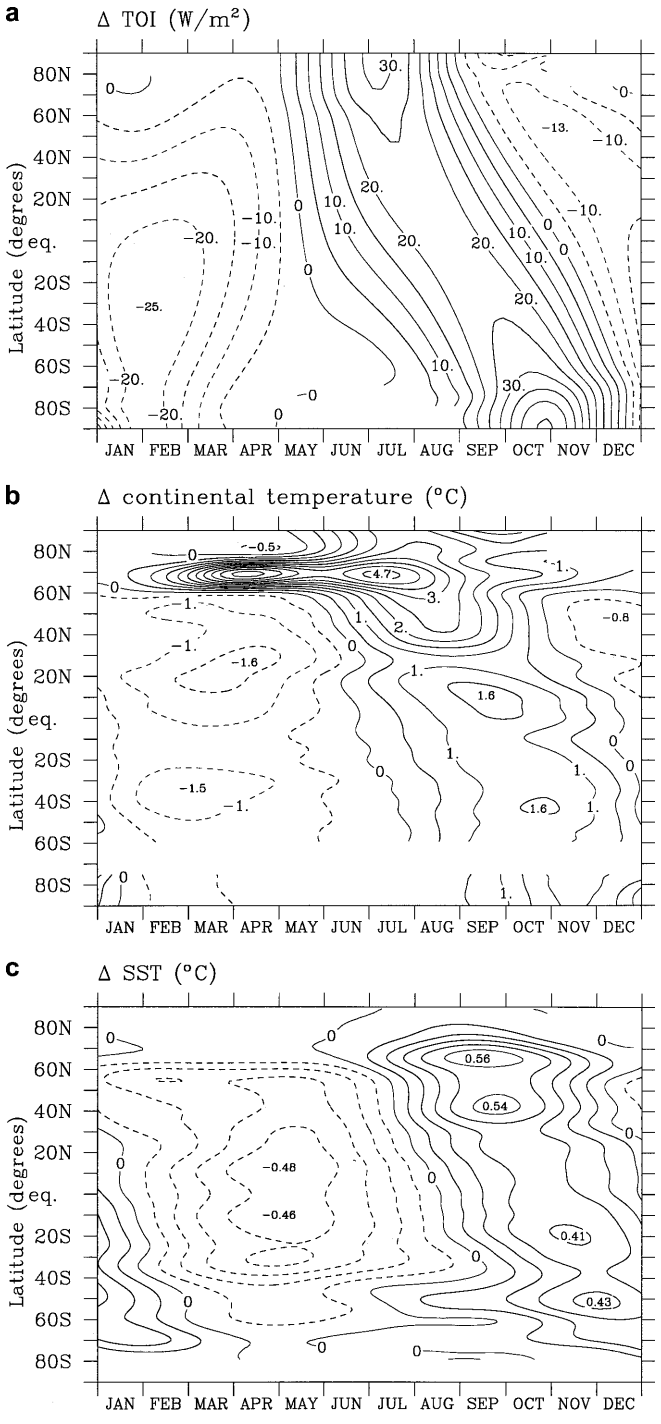

Fig. 6 Latitude-time distributions of the differences between 6 kyr BP and 0 kyr in **a** insolation at the top-of-the-atmosphere (in W/m^2), **b** simulated zonally averaged surface continental temperature (in °C) and **c** simulated zonally averaged SST (in °C)

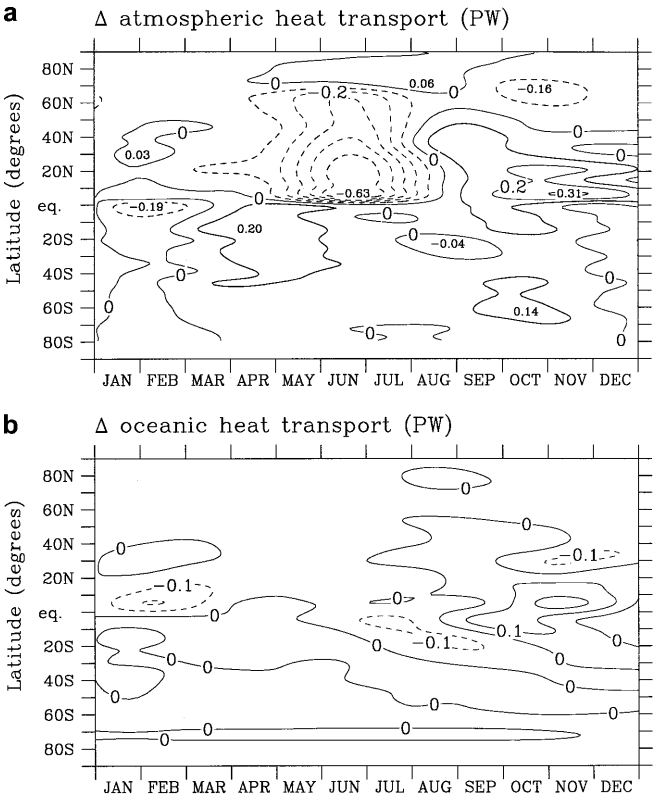

Fig. 7 Latitude-time distributions of the differences between 6 kyr BP and 0 kyr snapshot experiments in **a** atmospheric heat transport (dry static + latent) and **b** oceanic heat transport. Heat transports are expressed in PW and are positive northward

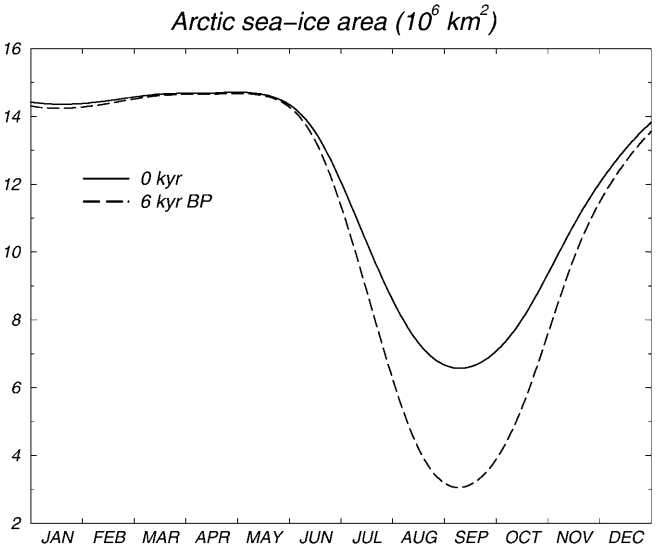

Fig. 8 Seasonal cycles of the Arctic sea-ice area (in 10^6 km^2) for 0 kyr and 6 kyr as simulated in snapshot experiments

north of 60°N. Indeed, the warm branch of North Atlantic circulation that goes up to 75°N is known to induce, in the real world, a strong axial asymmetry, the Norwegian climate being typically much milder than the Siberian one. On the other hand, reconstructions show that the largest vegetation shifts occurred in Northern Siberia (Prentice and Webb 1998; MacDonald et al. 2000), while there were much smaller in Scandinavia. This observation suggests that the mild maritime climate of Scandinavia is less sensitive to variations in summer solar radiation, a feature that is not captured by MoBidiC.

3.2.6 Precipitation

The model simulates small changes in the zonally averaged precipitation. North of 60°N, the 6 kyr precipitation is, in

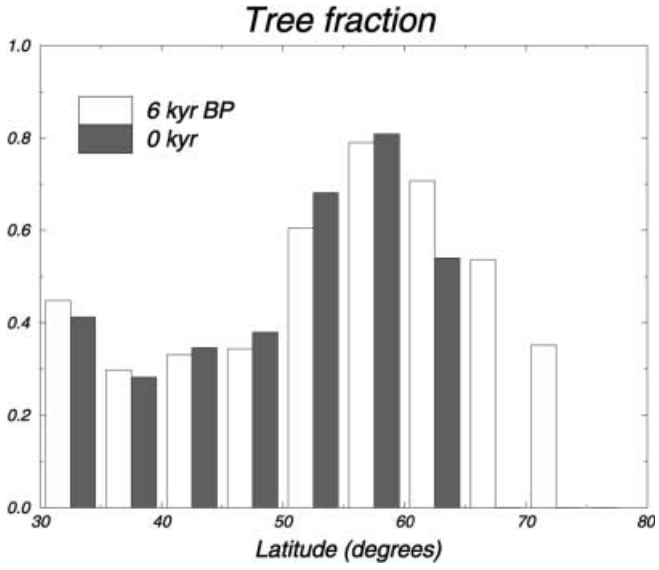

Fig. 9 Latitudinal distributions of the sub-grid scale tree fraction north of 30°N for 0 kyr and 6 kyr simulated in the snapshot experiments

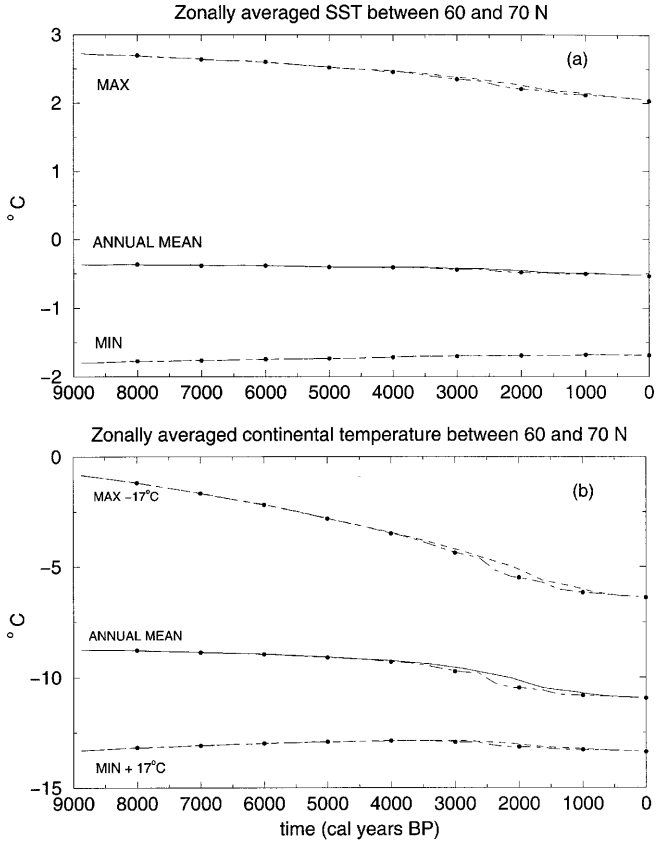

Fig. 10a, b Transient experiment AOV. Simulated evolutions of **a** the zonally averaged SST and **b** the zonally averaged continental temperature between 60 and 70°N over the last 9 kyr BP. Annual means (full lines) are plotted along with the maxima and minima of the 30-day running average (dashed lines). The *dash-dotted lines* represent the temperature evolutions in a transient experiment in which vegetation is imposed to be instantaneously in equilibrium with climate (AOV*). The *dots* represent the values obtained in corresponding equilibrium runs (see Sect. 4.2 for details)

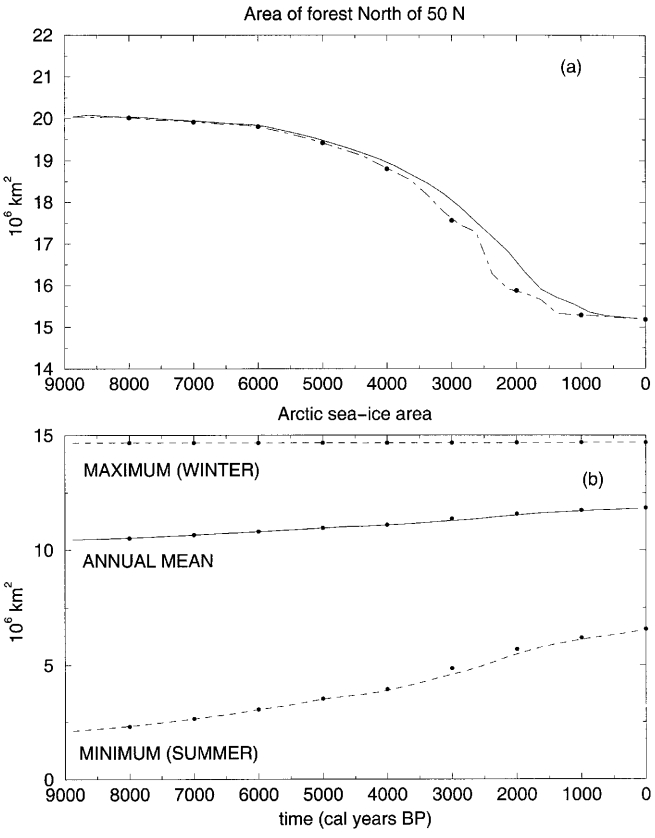

Fig. 11a, b Transient experiment AOV. **a** Time evolution of the area of forest north of 50°N (*solid line*). The *dash-dotted line* represents the evolution of boreal forest area obtained in a transient experiment in which vegetation is imposed to be instantaneously in equilibrium with climate (AOV*). **b** Time evolution of Arctic sea-ice area over the last 9 kyr BP. The annual mean (*solid line*) is plotted along with the annual maximum and minimum area (30-day average, *dashed lines*). In both figures, the *dots* represent the values obtained in corresponding equilibrium runs

annual mean, 0.08 mm/day larger than today, in response to the increase in evaporation in the Atlantic and Pacific oceans. The increase is largest in summer (0.3 mm/day). Such small differences are coherent with the GCM estimate of Foley et al. (1994) and certainly confirm that the treeline shift simulated by our model is thermally driven. Indeed, sensitivity studies show that the difference in precipitation simulated between 6 kyr and 0 kyr would be responsible, alone, for changes in boreal forest area no larger than about 0.2%. Hence, we conclude the GDD0 is clearly the dominant factor in driving the northern treeline shift.

3.3 Implications

According to these 6 kyr BP and preindustrial snapshot experiments, MoBidiC appears as a valid tool, complementary to GCMs, to study the non-linear interactions between climatic processes in the mid- and high latitudes, despite a possible oversensitivity of vegetation to the orbital forcing. In the intertropical regions, the simulated temperature pattern remain, in zonal average, in reasonable agreement with GCMs. In particular, the model correctly represents the impact of the astronomical forcing on the activity of the Hadley cells. However, the model does not simulate the slight continental cooling simulated by GCMs in intertropical continents. More fundamentally, it misses the important redistributions of heat and water-vapour between the oceans and the

Table 1 Description of the sensitivity experiments presented in this study

	$e \sin \tilde{\omega}$	ε	CO_2	Vegetation	Ocean–sea ice
AOV	BER78	BER78	T.Dome	Yes	Yes
AOV*	BER78	BER78	T.Dome	Yes	Yes
A	BER78	BER78	T.Dome	No	No
AO	BER78	BER78	T.Dome	No	Yes
AV	BER78	BER78	T.Dome	Yes	No
AOV-C	–0.0145	24.2316	T.Dome	Yes	Yes
AOV-P	BER78	24.2316	261	Yes	Yes
AOV-O	–0.0145	BER78	261	Yes	Yes
AOV-PO	BER78	BER78	261	Yes	Yes

All the experiments start from the same initial conditions, obtained from an equilibrium experiment using the 9 kyr BP astronomical parameters and a CO_2 concentration of 261 ppmv. The first series aims at studying the role of the different components (vegetation, ocean–sea ice). 'No' means that the subcomponent is fixed to its 9 kyr BP state. The second series aims at testing the role of the different forcings (astronomical forcing and CO_2). $e \sin \tilde{\omega}$ and ε are the precession parameter and the obliquity, respectively. They can be fixed to their 9 kyr BP value or computed using the analytical formulation of Berger (1978) (BER78). T.Dome means that the CO_2 concentration is obtained from a 3-rd order polynomial fit on the Taylor Dome ice core measured by Indermühle et al. (1999). AOV* is equivalent to AOV, except that in AOV* vegetation is forced to be instantaneously in equilibrium with climate

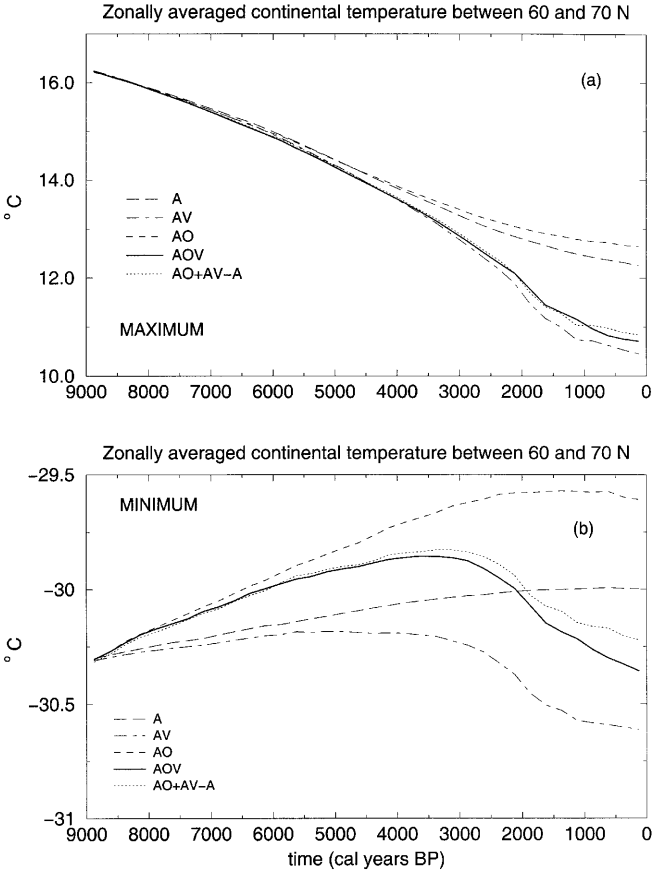

Fig. 12a, b Sensitivity of northern continental temperatures (between 60 and 70°N) to the presence of vegetation and oceanic feedbacks in the model. **a** Annual maximum (30-day running average), **b** annual minimum (30-day running average). Definitions of A, AO, AV and AOV are given in Table 11. The *dotted curve* represents the response of the system assuming no synergy between oceans and vegetation (see Sect. 4.3 for further details)

continents, yet clearly evidenced by the data. These limitations of our model are basically linked to its structure, which is not designed to represent monsoon dynamics satisfactorily. In the following sections, we take benefit of its advantageous computing cost and will focus on the transient aspect of vegetation–ocean–atmosphere interactions in the northern high latitudes throughout the last 9 kyr.

4 Holocene transient experiments

4.1 Standard experiment (AOV)

The standard experiment, hereafter referred to as AOV, is designed to study the transient behaviour of climate over the last 9 kyr using interactive ocean–sea ice (O) and vegetation (V). Initial conditions have been obtained by integrating the model under the 9 kyr BP seasonal distribution of insolation and a CO_2 concentration of 261 ppmv until equilibrium. The model integration is then carried out for 9000 years under the orbital and CO_2 transient forcings. The orbital parameters are computed according to Berger (1978). The atmospheric CO_2 concentration is taken from a third-degree polynomial best fit to the Taylor Dome ice-core data from Indermühle et al. (1999). For all experiments, the Greenland and Antarctic ice sheets are prescribed as today.

The simulated globally averaged annual mean temperature varies little. It increases from 14.60 to 14.65 °C between 9 kyr and 3 kyr BP, and then decreases back to 14.55 °C. However, in the northern high latitudes, and more specifically between 60 and 70°N, the model exhibits a clear cooling trend throughout the Holocene, especially in summer, both over oceans and continents (solid and dashed lines on Fig. 10). The trend is roughly gradual, with two noticeable features.

1. The variation is fastest between 4 and 1 kyr BP. This feature is associated with a hastening of the treeline shift, about 80% of the reduction of the boreal forest area occurring after 4 kyr BP (Fig. 11a), which is consistent with the reconstructions by MacDonald et al. (2000). This vegetation effect is enhanced by a

substantial increase in sea-ice area between 4 and 1 kyr BP (Fig. 11b) and a decrease in summer SSTs (Fig. 10a). As this will be developed more in depth in Sect. 4.4, this feature is essentially linked to the non-linear relationship that prevails between tree area and summer temperature. The phenomenon is thus in some way similar to the Sahara desertification simulated by Claussen et al. (1999), except that it does not present the same abruptness.

2. Winter continental temperatures between 60 and 70°N do not vary monotonously. Overall, the variations are very weak. They pass through a maximum about 3 kyr BP and decrease afterwards by 0.5 °C until the present day.

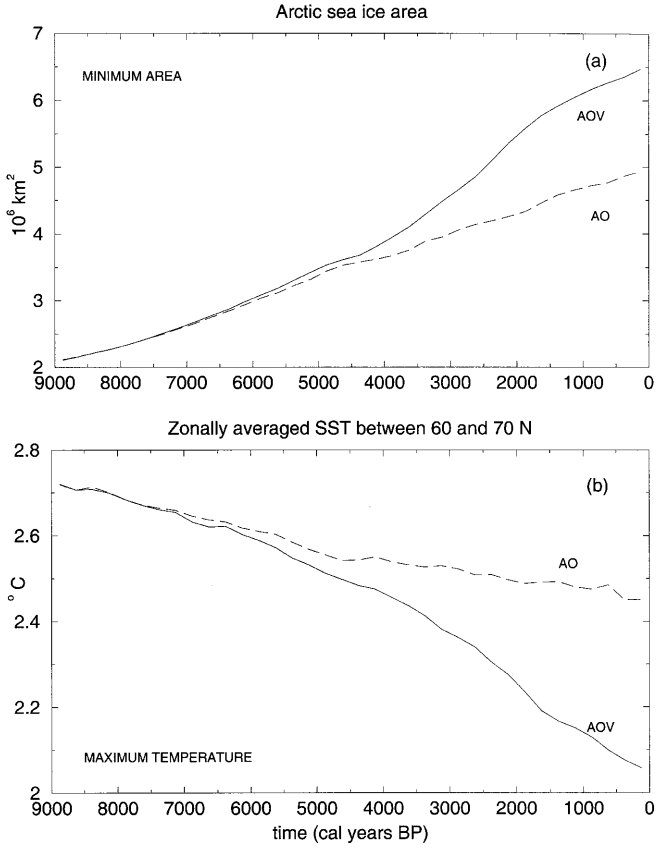

Fig. 13a, b Sensitivity of summer Arctic sea-ice area and SST to the presence of an active vegetation component in the model. **a** Minimum arctic sea-ice area (30-day running average); **b** maximum SST between 60 and 70°N (30-day running average). The meaning of AO and AOV are given in Table 1

The thermohaline circulation exhibits a slight slowdown throughout the Holocene, the NADW export into the Southern Ocean decreasing from 12.7 Sv to 12.4 Sv (not shown). Most of this decrease occurs between 9 and 6 kyr BP and is essentially a response to the increase in winter atmosphere temperature above convective areas (i.e., in our model, between 40 and 60°N) that reduces slightly the latent and sensible heat fluxes from the ocean to the atmosphere.

4.2 Deviation with respect to equilibrium

We performed eight additional equilibrium experiments, using astronomical and CO_2 forcings corresponding to 0 to 8 kyr BP by step of 1 kyr, in order to assess to what extent the climate simulated in the transient run deviates from the equilibrium responses to the external forcing. The corresponding results are represented by the dots plotted on Figs. 10 and 11. In this way, the deviation between transient states (solid and dashed lines) and the corresponding equilibrium states (dots) can be easily quantified.

In general, the change in forcing is sufficiently slow to allow the system to remain close to the equilibrium, especially before 4 kyr BP. Afterwards, the equilibrium climate changes more rapidly as the astronomical forcing evolves in time. The transient climate cannot adjust sufficiently quickly and a lag between transient and equilibrium climates appears. The largest deviation between transient and equilibrium states is noticed at 2 kyr BP. Transient climate then lags behind the equilibrium by about 200 years, so that high latitudes maximum continental temperature and SST are about 0.4 °C and 0.05 °C above their equilibrium values, respectively.

An additional sensitivity experiment, called AOV*, enabled us to determine whether this lag is due to the vegetation or to the ocean. Its experimental setup is the same as in the standard experiment, except that the vegetation is forced to be instantaneously in equilibrium with climate. The dash-dotted lines in Fig. 10a, b and 11a represent the time evolution of temperature and forest area obtained in this way. One can see that they go through the equilibrium points, showing that the system remains then very close to equilibrium, even between 4 and 1 kyr BP. This implies that the 200-year time lag observed in AOV, and vanishing in AOV*, originates from the vegetation response, which is consistent with

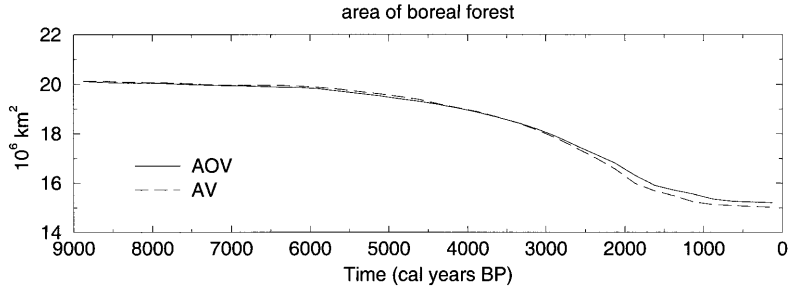

Fig. 14 Areas of tundra and cold desert throughout the Holocene as simulated in AV and AOV

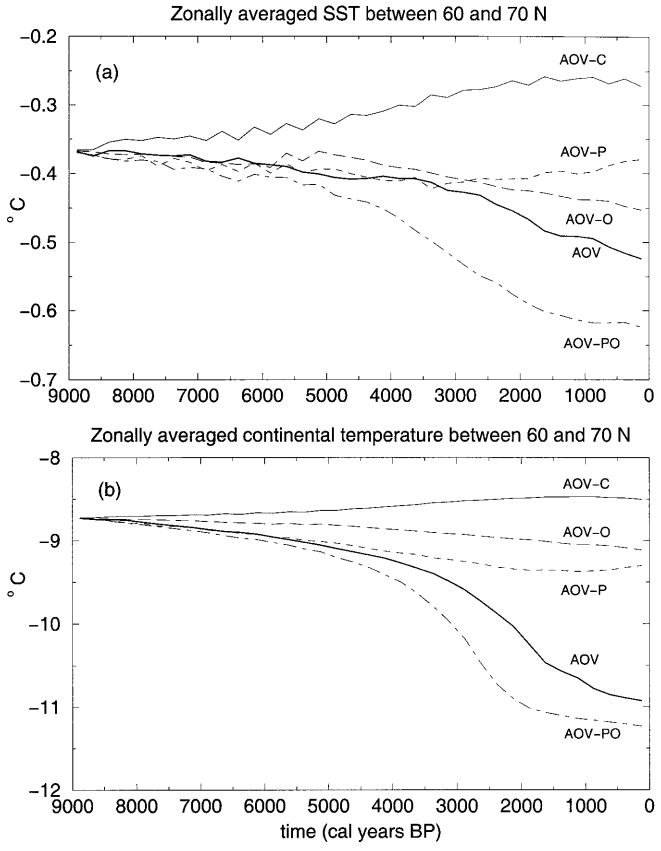

Fig. 15 Analysis of the effects of the different components of the forcing on **a** the zonally averaged, annual mean SST between 60 and 70°N and **b** the zonally averaged, annual mean continental temperature between 60 and 70°N

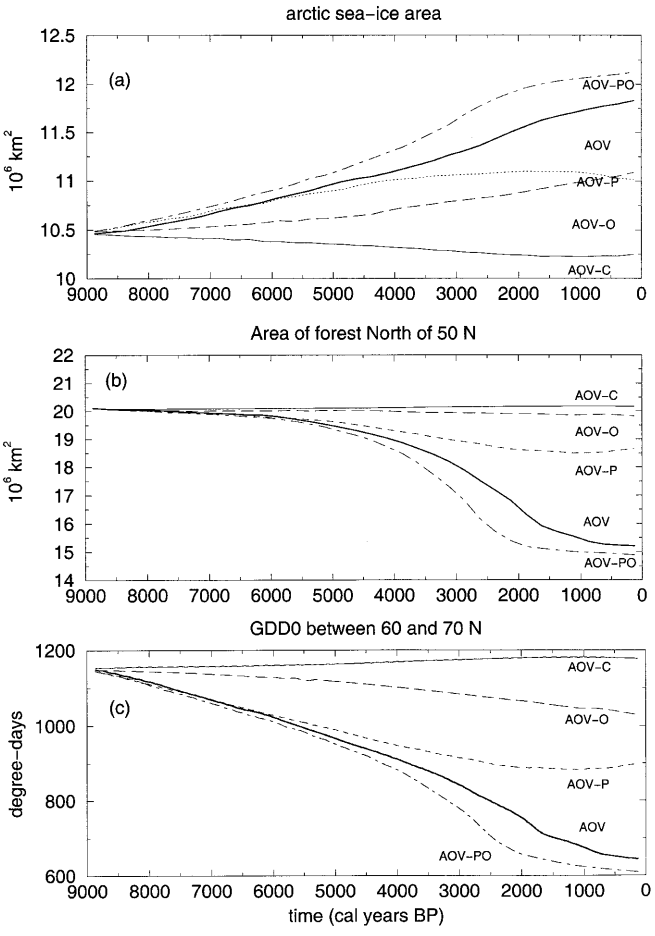

Fig. 16 Analysis of the effects of the different components of the forcing on **a** the Arctic sea-ice area, **b** the area of forest north of 50°N and **c** GDD0 index between 60 and 70°N

the characteristic time of vegetation renewal time at these latitudes. In contrast, the ocean introduces no lag, which suggests that SST variations are too small to give a significant role to the ocean thermal inertia.

4.3 Amplifying mechanisms and synergies

A series of sensitivity experiments has been carried out to study the individual roles of the ocean and the vegetation in the climatic changes simulated over the last 9 kyr BP. Experiments were designed in order to be consistent with the separation-factor technique of Stein and Alpert (1993), extended by Berger (2001) and Kubatzki et al. (2000) (Table 1). In experiment A (atmosphere only), the seasonal cycle of SST and sea-ice area as well as the distribution of the vegetation are kept constant to their 9 kyr BP equilibrium. In AV, ocean temperature and sea-ice cover are prescribed to their 9 kyr BP state, while vegetation is computed interactively by VECODE. In AO, the vegetation is fixed to its 9 kyr BP distribution, while ocean currents, surface temperature and sea-ice are computed by the ocean-sea-ice model. By comparing the results obtained in AV and AO with those from A, it is possible to assess the pure contributions of the vegetation (AV–A) and the ocean (AO–A) in amplifying (or possibly damping) the effects of the external forcing as simulated in A. Then, it is possible to identify potential synergies between vegetation and ocean. This synergy can be quantified by the additional deviation simulated between AOV and A with respect to the sum of the pure contributions of ocean and vegetation (AOV–A compared to (AV–A) + (AO–A)).

Figure 12 shows the simulated time evolution of continental temperature between 60 and 70°N in summer (a) and winter (b) for the different sensitivity experiments. In A, the model exhibits a gradual and monotonous trend. The evolution of summer continental temperature reflects quite linearly the external forcing variation, i.e. a decrease in June insolation by 44 W/m^2. In winter, variations in insolation are very small, but the effects of winter insolation increase at lower latitudes are communicated to the high latitudes through a very slight increase in atmospheric heat transport (about 0.05 PW). Introducing the ocean (AO) slightly damps the summer continental cooling trend, while it strengthens its winter warming trend. Over the entire time interval, this effect

amounts to a few tenths of degrees both in winter and summer. The tendency of the ocean to damp astronomically induced summer temperature variations on the continents was already noticed by Ganopolski et al. (1998) and Braconnot et al. (2000) when comparing 6 kyr BP and 0 kyr snapshot simulations. This results from the thermal inertia of the ocean that introduces a lag between the seasonal cycle of insolation and the oceanic response. Because of this lag, the mid-latitudes May SST in the Northern Hemisphere increase throughout the Holocene by about 0.5 °C, although May insolation experiences little variations. As a consequence of this warming, continental snow melting is enhanced with respect to A, leading to warmer summers in AO. The strengthening of the continental winter warming trend caused by the ocean can be explained in a similar way. The increase in summer and autumn insolation in the mid-latitudes (between 30 and 60°N) produces an increase in winter SST by about 1 °C. Because of the resulting enhanced meridional temperature gradient, the atmospheric heat transport to the high latitudes is strengthened, which induces a warming of the continents north of 60°N.

Interactive vegetation (AV) also produces important alterations of the temperature trends. It amplifies the summer cooling and introduces a winter cooling between 4 kyr BP and 0 kyr. Let us remember that the impact of vegetation is expected to be mainly through the albedo of snow-covered land surface. The impact of vegetation on summer temperatures is therefore not straightforward because there is very little snow during this season (the maximum continental temperature, as plotted in Fig. 12, occurs around the 15th July). Actually, due to its effect on snow albedo, expansion of tundra strongly reduces the snow-melting rate in spring. Thaw is consequently delayed which, considering the one month thermal inertia of the continents, explains lower July temperatures.

Finally, comparing AOV with AV and AO reveals that, in this model, the contributions of the ocean and vegetation sum up roughly linearly. Indeed, the dotted curves, representing AO + (AV–A), i.e. assuming that the pure contributions of oceans and vegetation to the continental temperature sum up linearly, are very close to AOV. This result suggests a weak synergy between vegetation and ocean during the Holocene, which substantially differs from the conclusions drawn out by Ganopolski et al. (1998) with CLIMBER. It is then interesting, at this stage, to attempt to identify the reason for this weak synergy.

The physical interpretation of the vegetation–ocean synergy is mainly based on the idea that the spring cooling related to the treeline recession reduces the sea-ice melting rate (contribution of the southward displacement of the treeline to the ocean cooling). As a consequence, summer sea-ice area increases, which further reduces summer continental temperatures and eventually accelerates the vegetation shift (contribution of the ocean cooling to the vegetation shift). The difference in synergy strength exhibited between CLIMBER and MoBidiC may lie either in the contribution of the vegetation shift to the ocean cooling, either in the contribution of the ocean to vegetation changes, or in both. Figure 13 shows that the southward displacement of the treeline causes a further increase in sea-ice area by about 1.5×10^6 km^2 in AOV with respect to AO, while maximum SSTs (i.e. around the 20th August) between 60 and 70°N are 0.4 °C colder by the end of the run. Although significant, the contribution of vegetation to the ocean-sea-ice system is here less than in CLIMBER, where the vegetation shift causes an additional increase in northern sea-ice by 2.5×10^6 km^2 between 6 kyr BP and 0 kyr. Focusing now on the contribution of the ocean cooling on the vegetation shift, one notices that the latter is similar in AV and in AOV (Fig. 14), which suggests that the variations simulated in the ocean temperature and sea-ice area do not significantly alter the behaviour of the treeline. Actually the effect of the ocean on the boreal forest is quite opposite to what would be expected for a positive synergy, the simulated expansion of tundra and cold desert throughout the Holocene being reduced when the ocean is taken into account (i.e. the area of boreal forest decreases less). This feature results from the increase in mid-latitude SSTs in spring and early summer, that is communicated to the atmosphere. As a consequence, the simulated spring SST increase tends to increase the snow melting rate, thereby counteracting the effect of insolation on vegetation. This is not the case in CLIMBER, in which the vegetation shift is slightly larger in AOV than in AV. This is probably because in contrast to MoBidiC, CLIMBER exhibits much less winter sea-ice at 6 kyr BP than today. In turn, this promotes earlier sea-ice and snow melting which eventually benefits the boreal vegetation. Hence, we conclude that sea-ice sensitivity, especially in winter, is probably the key point of the difference between both models in ocean-vegetation synergy strength.

4.4 Decomposition of the external forcing

In this section, we present sensitivity studies designed to assess the respective influences of the different components of the external forcing. Two components basically contribute to the external forcing: the orbital forcing and the CO_2. Hence, we first performed two experiments: in AOV-PO, only the orbital forcing is applied and CO_2 is kept constant to its value of 261 ppmv throughout the run. Conversely, in AOV-C, CO_2 varies as in AOV and orbital parameters are kept constant to their 9 kyr values. Then, two additional sensitivity experiments were performed to assess the individual contributions of precession and obliquity in the orbital forcing. These experiments are referred to as AOV-P and AOV-O. In AOV-P, only the precession parameter (which is a function of eccentricity and the longitude of perihelion) varies while obliquity is fixed. The reverse configuration

is applied in AOV-O. All of these experiments are defined in Table 1.

Figure 15 illustrates the effects of the individual forcing components on the zonally averaged SST and continental temperatures. It follows several observations highlighting the non-linearity of the climatic system:

1. The effect of introducing CO_2 variations is not the same depending on whether variations in the orbital forcing are taken into account or not. Indeed, under a constant astronomical forcing (experiment AOV-C), the CO_2 is responsible for a 0.3 °C increase in annual mean continental temperature (between 60 and 70°N) and for a 0.1 °C increase in SST. When changes in the orbital forcing are taken into account, introducing the CO_2 may temporarily lead to differences as high as 1 °C on the continent, especially between 4 and 1 kyr BP (compare AOV-PO and AOV in Fig. 15b). This suggests that throughout the Holocene, the high-latitude climate may have temporarily passed through episodes of high sensitivity to CO_2.
2. Considered alone, obliquity and precession have little impact on annual mean temperatures. For example, obliquity is responsible for a decrease of 0.1 °C in annual mean SST between 60 and 70°N and of 0.4 °C on the annual mean continental temperature. Precession has a slightly weaker impact than obliquity on SST, while its impact on continental temperatures is larger. The impact of precession on annual mean temperatures is on its own a consequence of the non-linear response of the climate. Indeed, precession does not affect annual mean insolation (216.0 W/m^2 at 65°N). The annual mean cooling between 60 and 70°N then results from an increase in the annual mean surface albedo of the continents (about 3%), due to the expansion of both the snow field and tundra, which are sensitive to seasonal climatic variations (see Sect. 3.2.5).
3. Finally, it turns out that both precession and obliquity are needed to produce substantial climatic changes in the high latitudes during the Holocene. In particular, the cooling simulated in AOV-PO (about 2.2 °C in annual mean) is much larger that the sum of individual contributions of precession and obliquity (about 1 °C).

Part of these results is related to the non-linear relationship between the GDD0 index and the tree fraction in the high latitudes. Indeed, sensitivity studies made with MoBidiC show that the tree fraction is particularly sensitive to GDD0 in a range extending from 400 to about 1100 degree-days. (Brovkin et al. 2002). Above a GDD0 index of 1100 degree-days, the tree fraction is close to its maximum and is much less sensitive to small climatic variations. At 9 kyr BP, the simulated GDD0 between 60 and 70°N amounts to 1150 degree-days (Fig. 16c). Throughout the Holocene, precession and obliquity contribute to decrease this value, but applied independently, they have a minor impact on the tree fraction. On the contrary, their combined impact is significant because GDD0 is then in a range where vegetation is much more sensitive to climate. In particular, this explains why small changes in CO_2 concentration have an important impact on the treeline at about 2 kyr BP (compare AOV-PO with AOV), because GDD0 is then equal to about 700 degree-days, i.e. a value for which the tree fraction is the most sensitive to temperature.

5 Discussion and conclusion

The simulation of the temporal evolution of climate over the last 9 kyr requires simplifications with respect to AOGCMs in order to spare computing time. It was also necessary to couple the most relevant components of the climatic system at that time scale, including the atmosphere, the ocean, sea ice and terrestrial vegetation. The solution that has been retained here was to adopt a sectorial structure to represent the Earth's surface. Despite this important simplification, MoBidiC presents a sensitivity to the orbital forcing comparable to GCM results. The simulated oceanic and continental temperature differences between 6 kyr BP and 0 kyr snapshot equilibria are consistent with earlier GCMs results, especially at high latitudes.

On this basis, it has been possible to produce reliable insights on the transient climate behaviour over the last 9 kyr BP, with a special focus on the northern high latitudes. A first question was to determine to what extent climate is close to equilibrium during this period. From comparisons performed between equilibrium and transient experiments, we found that the deviation is usually negligible, except between 4 and 1 kyr BP. It is indeed during this period that, in agreement with the data, most of the boreal vegetation reorganisations take place, which implies a characteristic time of about 200 years. However, such reorganisations do not present the abrupt character that characterised, for example, the Sahara desertification. This lead us to conclude that, in contrast to the precipitation–vegetation feedback operating in the tropics, the temperature–vegetation feedback is not sufficiently intense to trigger abrupt events in response to the smooth orbital forcing.

Before 7 kyr BP, model results should be considered with more caution. Indeed, one must keep in mind that the persistence of the Laurentide ice sheet until 8 kyr BP (Hughes et al. 1981; Peltier 1998; Lambeck et al. 2000) as well as the long renewal time of ocean deep-water certainly impacted on the climate in the northern high latitudes during this period. For example, the slight slowdown of the thermohaline circulation simulated between 9 and 6 kyr BP was obtained without considering the meltwater flow that originated from the residual Laurentide ice sheet during the early Holocene. Also, Ruddiman and Mix (1993) reported an important SST increase in the North Atlantic between 9 and 8 kyr BP and similarly, diatom-based reconstructions suggest

a decrease in sea-ice coverage between 9 and 7 kyr BP (Koç et al. 1993). Such features, not predicted in our simulations, are likely to result from the end of the glaciation. As a consequence, we estimate that robust conclusions about the early Holocene climate would require much longer simulations covering the deglaciation history, and including either a prescribed or an interactive model of the ice sheets.

Two series of sensitivity experiments enabled us to learn more about the mechanisms involved in the Holocene climatic changes in the northern high latitudes. The feedback analysis revealed that the ocean and vegetation have opposite impacts on summer continental temperature trends. Due to its thermal inertia that introduces a 2.5-month lag between insolation and SST, the ocean reduces the summer continental cooling trend. On the contrary, the southward shift of the treeline (i.e. expansion of tundra) resulting from shorter and colder growing seasons, enhanced the summer cooling trend, both on the ocean and continent. These counteracting influences of ocean and vegetation on summer continental temperatures can readily be identified by analysing the pure contributions of vegetation and ocean, i.e. by separately activating the vegetation and ocean models, the remaining component being prescribed. Counteracting influences subsist when both vegetation distribution and ocean temperature are calculated, the impact of vegetation being then by far dominant. The model exhibits a weak synergy between vegetation and ocean, likely attributable to the rather weak sensitivity of winter sea-ice to the astronomical forcing.

We have seen that this result is opposite to some earlier works. Actually, assessing the ocean–vegetation synergy is a complex matter because it requires us to simulate, in a quantitative manner, the mutual interactions between ocean and vegetation. Regarding this question, an interesting problem, still unsolved, is to assess the exact sensitivity of ocean temperatures at high latitudes to orbital forcing. Indeed, although we stressed that the SST changes simulated here are quantitatively compatible with previous results of snapshot AOGCMs, two arguments arising from data analysis suggest that they can be underestimated. First, according to some reconstructions, summer Arctic SST could have been 4 °C warmer at 6 kyr BP than today (Koç et al. 1996; Kerwin et al. 1999), i.e. much more than predicted by models. Second, we showed with the forcing-decomposition analyses that obliquity alone produces SST changes of about 0.1 °C. Such small changes do not satisfactorily explain the strong 40 kyr signal (i.e. obliquity signal) found in the deuterium excess record from Antarctica (Vimeux et al. 1999, 2001) suggesting that in some manner obliquity exerted a significant control on annual mean SSTs, at least in the Southern Hemisphere.

As a last result, our forcing analysis leads us to suggest that the high-latitude climate may have passed through an episode of high sensitivity to the external forcing when the expansion of tundra took place (between 4 and 1 kyr BP). At this stage, this result cannot yet be regarded as definitely conclusive because of the lack of resolution in MoBidiC. However, its two main implications: (1) both obliquity and precession are required to enable the treeline shift and (2) a 20 ppmv change in CO_2 may have locally produced temperature changes as high as 1 °C; are certainly two interesting subjects for the GCM simulations.

Acknowledgements We warmly thank Victor Brovkin (Potsdam Institute for Climate Impact Research, Germany) for providing us with the computer code of VECODE, as well as for his assistance to implement it into MoBidiC. Discussions with Elsa Cortijo, Françoise Vimeux and Pascale Braconnot during a visit to LSCE were of great benefit. MC and TF are Research Fellow and Research Associate with the Belgian National Fund for Scientific Research (FNRS), respectively. Part of this work was done within the scope of the Environment and Climate Program of the European Commission (Contract ENV4-CT97-0643) and the Impulse Program "Global Change" (Contract GC/DD/13, Belgian State, Prime Minister's Office, Federal Office for Scientific, Technical and Cultural Affairs).

Appendix

Model description

MoBidiC is a global, 2.5-dimensional climate model with representations of the atmosphere, the oceans, sea ice, the land surface and terrestrial vegetation. It has a latitudinal resolution of 5°, and each latitudinal band is divided into two continental sectors (Eurasia–Africa and America) and three oceans (Atlantic, Pacific and Indian). The longitudinal extent of the sectors (ocean and continents) as well as the altitude of the continents are prescribed according to the ETOPO 5 (1986) dataset. Each continental sector can be partly covered by snow, and similarly, each oceanic sector can be partly covered by sea ice (with a possible snow layer).

The atmospheric dynamics is represented by a zonally averaged, two-level quasi-geostrophic (QG) potential vorticity model written in pressure coordinates (Sela and Wiin-Nielsen 1971), with the numerical implementation given in Gallée et al. (1991). The prognostic variables for the atmosphere are the QG potential vorticity at 250 hPa and 750 hPa. The atmospheric model allows to diagnose temperature at 500 hPa and wind vorticity at 250 hPa and 750 hPa, the latter being linearly extrapolated to the surface to compute the zonal surface wind velocity. The prognostic equations for each vertical level are closed by parametrising the meridional transport of potential vorticity due to the baroclinic activity using a diffusive formulation.

In order to reduce the limitations inherent to the QG formalism between the tropics, Gallée et al. (1991) followed Held and Hou (1980) and Peng et al. (1987) in parametrising the vertically integrated heat transport ($\int_p \bar{v}\bar{\theta}dp$) associated with the mean meridional circulation. We introduce here an additional parametrisation of the vertically integrated meridional momentum transport by the Hadley cell ($\int_p \bar{u}\bar{v}dp$) in function of the latitude φ, that remains consistent with the theory developed by Held and Hou (1980) in order to enhance the representation of the trade winds:

$$\int_p \bar{v}\bar{u}dp = -\frac{C_u y^{*2}}{S_h}\int_p \bar{v}\bar{\theta}dp \ , \qquad (1)$$

where C_u is an empirical constant (see Table 2 for constant and parameter values), $y^* = (\varphi - \varphi_0)/(\varphi_h - \varphi_0)$ where φ_0 and φ_h are the latitude of the intertropical convergence zone and the poleward latitudes of the Hadley cells, respectively, calculated according to Gallée et al. (1991), and S_h is the relative difference in potential temperature between the surface and the tropopause, the pressure of which is calculated as a function of the zonally averaged surface

Table 2 Constant and parameter values used in the model

Atmosphere		
σ	2.5×10^{-6} m^4 s^2 kg^{-2}	Static stability parameter
A	0.6×10^{-6} s^{-1}	Internal friction coefficient (Sela and Wiin-Nielsen 1971)
ε	3.8×10^{-6} s^{-1}	Surface drag coefficient
C_K	2.1×10^{7} m^2 s^{-1}	Parameter for the meridional heat transport by the mean meridional circulation (MMC) (Gallée et al. 1991)
C_q	10^{-13} kg J^{-1}	Parameter for the meridional water-vapour transport by the MMC
C_u	0.5×10^{-14} m s^{-1} K^{-1}	Parameter for the meridional momentum transport by the MMC
τ	0.72	Cloud optical depth (adapted from Chou et al. 1981)
Land surface		
r_s	0.75	Surface relative humidity
a	0.7×10^{-3} m s^{-1}	Parameter for evaporation (adapted from Saltzman 1980)
b	4.5×10^{-3} m s^{-1}	Parameter for evaporation (adapted from Saltzman 1980)
α_T	0.12	Albedo of snow-free trees
α_G	0.25	Albedo of snow-free grass
α_D	0.35	Albedo of snow-free desert
$\alpha_{tundra,fs}$	0.83	Maximum snow albedo over tundra for frozen snow
$\alpha_{tundra,ms}$	0.70	Maximum snow albedo over tundra for melting snow
α_{taiga}	0.40	Snow albedo over taiga
B	0.321×10^{-6} W m^{-2} K^{-1}	Subsurface heat-storage coefficient
k_s	0.3 W m^{-1} K^{-1}	Thermal conductivity of snow
Sea ice		
S_{ice}	4 psu	Salinity of sea ice
k_i	2.04 W m^{-1} K^{-1}	Thermal conductivity of sea ice
h_0	1 m	Instantaneous thickness of new lead ice (Harvey 1988)
f*	0.13	Minimum permitted lead fraction for thin ice (adapted from Harvey 1988)
τ_1	3 m	Characteristic sea-ice thickness for lead fraction parametrisation (Harvey 1988)
$\alpha_{si,max}^{0}$	0.75	Maximum albedo of sea ice
$\alpha_{si,min}^{0}$	0.40	Minimum albedo of sea ice
Ocean		
A_M	2×10^{5} m^2 s^{-1}	Horizontal viscosity
μ	1×10^{-3} m^2 s^{-1}	Vertical viscosity
A_H	1.2×10^{3} m^2 s^{-1}	Horizontal diffusivity
κ	0.7×10^{-4} m^2 s^{-1}	Vertical diffusivity
γ	10 s	Closure parameter for downsloping flow (Campin and Goosse 1999)
ε	0.5	Closure parameter as in eq. (9) of Wright and Stocker (1992)
Flx	1 Sv	Intensity of the subpolar gyre (Crucifix et al. 2001)

temperature according to Sellers (1983). The angular momentum transport obtained in this way is about 2×10^{19} kg m^2 s^{-1} at 30°N and 30°S, which is consistent with usual estimates (Satoh et al. 1995). This transport induces an additional zonal surface wind, u_{mmc}, that is added to the one computed by the quasi-geostrophic model. This wind is determined assuming that the vertically integrated zonal momentum transport by the mean meridional circulation is solely compensated by surface stress:

$$u_{mmc} = -\frac{1}{aP\varepsilon\cos^2\varphi}\frac{\partial\cos^2\varphi\int_p \bar{v}\bar{u}dp}{\partial\varphi} \quad , \qquad (2)$$

where a is the Earth's radius, $P = 500$ hPa is the thickness of each atmospheric layer and ε is the surface drag coefficient.

The surface temperature of each continental surface type is considered as a prognostic variable and is derived from the surface heat balance parametrised as in Taylor (1976), assuming a constant subsurface storage coefficient B.

The radiative transfer is computed by dividing the model atmosphere into 10–15 layers, the exact number of which depending on the surface pressure over each surface type (Bertrand 1998; Bertrand et al. 1999). The solar radiation scheme is an improved version of the code described by Fouquart and Bonnel (1980). The longwave radiation is computed according to the Morcrette (1984) wide band formulation of the radiation equation. In the troposphere, the vertical temperature profile required by this radiative scheme is determined by assuming that the product of the static stability parameter σ and the pressure remains constant along the vertical. The stratosphere is supposed to be isothermal. Near the surface, the temperature lapse rate is modified so that the air has the same temperature as the surface. This lapse rate is used to compute the convective vertical sensible heat transport from the surface to the atmosphere according to the formulation of Saltzman and Ashe (1976). Specific humidity, q, is considered as a diagnostic variable: its surface value is determined from the surface temperature and a prescribed surface relative humidity. The vertical profile of specific humidity obeys the Smith (1966) relationship linking the specific humidity at a pressure p to its value at a reference level (pressure p_R): $q(p) = q(p_R)(p/p_R)^{\lambda}$, the seasonal and meridional distribution of λ being inferred from the present-day climatology of Oort (1983). The reference level is either the surface or the top of a possible inversion layer, the latter being then considered of constant specific humidity. Clouds are prescribed. They are represented by a single effective layer, with the base and the top pressures given by Ohring and Adler (1978). The seasonal and meridional distribution of cloudiness is taken from Warren et al. (1986), and the cloud optical depth is prescribed.

The albedo of a snow-free continental area is computed as the weighted average of the albedos of desert (α_D), grass (α_G) and trees (α_T). A similar method applies over the snow field where the model distinguishes between the albedo of snow-covered taiga (α_{taiga}) and snow-covered tundra (α_{tundra}). Additional corrections account for the effect of the Sun zenithal distance and snow precipitation frequency (Gallée et al. 1991).

Evaporation is computed from a bulk formulation depending on surface temperature, vertical sensible heat flux, surface wind velocity, surface pressure and water availability as in Saltzman (1980), although the empirical parameters a and b used by

Saltzman in his Eq. (14) have been somewhat adapted. Water availability is set equal to 1 (i.e. the maximum) over the ocean. It is a function of surface temperature over sea ice, continental ice and snow, and it depends on the precipitation–evaporation budget over the continents (Gallée et al. 1991).

The zonally averaged precipitation is derived from the zonally averaged evaporation and the vertically integrated water-vapour (WV) meridional transport assuming a steady state approximation for the global WV content. The vertically integrated WV transport ($\int_p \overline{v}\overline{q}dp$) is parametrised in a way consistent with the formulation of atmospheric dynamics assuming a transport by the baroclinic activity (diffusion) and by the mean meridional circulation:

$$\int_p \overline{v}\overline{q}dp = -\frac{K_1 + K_3}{2}\frac{\partial \int_p \bar{q}dp}{a\partial\varphi} - \frac{C_p C_q \bar{q}_{pbl}}{S_h}\int_p \bar{v}\bar{\theta}dp \ , \qquad (3)$$

where K_1 and K_3 are the exchange coefficients of the potential vorticity transport at 250 and 750 hPa, respectively (Gallée et al. 1991), $\int_p \bar{q}dp$ is the vertically integrated, zonally averaged specific humidity, $\bar{q}_{pbl}$ is the mean specific humidity in the first 150 hPa above the surface, C_p is the heat capacity of dry static air at constant pressure and C_q is an empirical parameter.

The zonally averaged precipitation that is computed in this way for each time step and each zonal band is distributed over the three oceanic basins and the two continents with ratios derived from the statistics by Jaeger (1976). An additional correction applies over the ice sheets in order to take the desert–altitude effect into account (Gallée et al. 1991). Finally, runoff is implicitly represented by multiplying the precipitation over the oceans such that the freshwater budget over the ocean is globally zero.

Within each individual oceanic basin (Atlantic, Pacific and Indian), the ocean model is based on the zonally averaged form of the multi-level, primitive-equation ocean model of Bryan (1969) and Semtner (1986). This model is extensively described in Hovine and Fichefet (1994) except for some improvements given hereafter. The east–west pressure difference which arises from averaging the momentum equations is taken to be proportional to the meridional pressure gradient as in Wright and Stocker (1992). In the Northern Hemisphere, lateral exchanges of heat and salt between the Atlantic and Pacific basins are permitted between 85 and 90°N. The zonally averaged topography is derived from ETOPO 5 (1986) and the Bering Strait is assumed to be 50-m deep. In the Southern Hemisphere, the three basins are interconnected between 40 and 65°S, where zonal advection and diffusion are represented. The Drake Passage and the Indian–Pacific connection are 4000 m deep, while the Atlantic and Indian basins are interconnected over the whole ocean depth (5000 m). The resolution of the baroclinic mode of the ocean is based upon an implicit treatment of vertical advection, viscosity and Coriolis terms. The numerical treatment of the scalars (potential temperature, salinity and tracers) is implicit on the vertical and explicit on the horizontal. The vertical diffusivity K_v is prescribed except when the vertical density profile is diagnosed to be unstable. In this latter case, vertical diffusivity is enhanced to 10 $m^2 s^{-1}$ to account for convection (Goosse and Fichefet 2000). The model also uses a sub-polar gyre parametrisation between 50 and 75°N in the Atlantic Ocean in order to improve the North Atlantic Deep Water properties (Crucifix et al. 2001). Likewise, a downsloping flow scheme based on Campin and Goosse (1999) is implemented along Antarctica. The value of parameter γ used in Campin and Goosse's (1999) parametrisation is given in Table 2.

A simple thermodynamic–dynamic sea-ice model is coupled to the ocean model. It is based on the zero-layer thermodynamic model of Semtner (1976), with the modifications introduced by Harvey (1988, 1992). The value of the parameters f^* and h_0 recommended by Harvey (1988) were adjusted to optimise the seasonal cycle of sea ice, the other parameter values being retained. The one-dimensional meridional ice advection scheme of Prather (1986) is also implemented with prescribed meridional ice velocities from Harvey (1988). Finally, the sea-ice albedo varies between 0.40 and 0.75 depending on the surface temperature, the minimum albedo being reached when the temperature is equal to 0 °C.

The atmosphere, sea-ice and ocean components are synchronously coupled with a time step of two days. For the simulations presented here, MoBidiC was also interactively coupled to the dynamical vegetation scheme VECODE (Brovkin et al. 1997). This model is based on a continuous bioclimatic classification which describes vegetation as a composition of simple plant functional types (trees and grass). Equilibrium tree and grass fractions are parametrised as a function of climate expressed as a sum of degree-days (GDD0) and annual precipitation. The model assumes that, under a changing climate forcing, the vegetation cover evolves towards a new equilibrium with the modified climate. The characteristic time scale of the living biomass is determined from the carbon-cycle component of VECODE (about 80 to 100 years for trees in the northern high latitudes).

References

Berger A (1978) Long-term variations of daily insolation and Quaternary climatic changes. J Atmos Sci 35: 2362–2367

Berger A (1983) Astronomical approach of paleoclimatic variations. Actes Coll AGSO Bordeaux, France, 34: 7–26

Berger A (2001) The role of CO_2, sea-level and vegetation during the Milankovitch-forced glacial-interglacial cycles. In: Proc Geosphere–Biosphere Interactions and Climate. Cambridge University Press, New York (in press)

Bertrand C (1998) Climate simulation at the secular time scale. PhD Thesis Institut d'Astronomie et de Géophysique G. Lemaître Université catholique de Louvain, Belgium, 208 pp

Bertrand C, van Ypersele JP, Berger A (1999) Volcanic and solar impacts on climate since 1700. Clim Dyn 15: 355–367

Braconnot P, Joussaume S, Marti O, de Noblet N (1999) Synergistic feedbacks from ocean and vegetation on the African monsoon response to mid-Holocene insolation. Geophys. Res Lett 26(16): 2481–2484

Braconnot P, Marti O, Joussaume S, Leclainche Y (2000) Ocean feedback in response to 6 ky BP insolation. J Clim 13: 1537–1553

Brovkin V, Ganopolski A, Svirezhev Y (1997) A continuous climate-vegetation classification for use in climate-biosphere studies. Ecol Modell 101: 251–261

Brovkin V, Levis S, Loutre MF, Crucifix M, Claussen M, Ganopolski A, Kubatzki C, Petoukhov V (2002) Stability analysis of the climate-vegetation system in the northern high latitudes. Clim Change (in press)

Bryan K (1969) A numerical method for the study of the circulation of the world ocean. J Comp Phys 4: 347–376

Bush AB (1999) Assessing the impact of Mid-Holocene insolation of the atmosphere–ocean system. Geophys Res Lett 26(1): 99–102

Campin JM, Goosse H (1999) Parametrization of density-driven downsloping flow for a coarse-resolution ocean model in z-coordinate. Tellus 51A: 412–430

Chou S, Currou R, Ohring G (1981) The effects of surface evaporation parametrization on climate sensitivity to solar constant variations. J Atmos Sci 38: 931–938

Claussen M, Gayler V (1997) The greening of Sahara during the mid-Holocene: results of an interactive atmosphere–biome model. Global Ecol Biogeogr Lett 6: 369–377

Claussen M, Kubatzki C, Brovkin V, Ganopolski A (1999) Simulation of an abrupt change in Saharian vegetation in the mid-Holocene. Geophys Res Lett 26(14): 2037–2040

Claussen M, Mysak LA, Weaver AJ, Crucifix M, Fichefet T, Loutre MF, Weber SL, Alcamo J, Alexeev VA, Berger A, Calov R, Ganopolski A, Goosse H, Lohman G, Lunkeit F, Mokhov I, Petoukhov V, Stone P, Wang Z (2001) Earth system models of intermediate complexity: closing the gap in the spectrum of climate system models. Clim Dyn (in press)

Crucifix M, Tulkens P, Berger A (2001) Modelling abrupt climatic change during the last glaciation. In: Seidov D, Haupt BJ, Maslin M (eds.) The oceans and rapid climate change: Past, present and future. Vol 126 of Geophysical Monograph. American Geophysical Union, pp 117–134

de Vernal A, Hillaire-Marcel C (2000) Sea-ice cover, sea-surface salinity and halo-/thermocline structure of the northwest North Atlantic: modern versus full glacial conditions. Quat Sci Rev 19(1–5): 65–85

Doherty R, Kutzbach J, Foley J, Pollard D (2000) Fully coupled climate/dynamical vegetation model simulations over Northern Africa during the mid-Holocene. Clim Dyn 16: 561–573

ETOPO 5 (1986) Global 5′ × 5′ depth and elevation. Available from National Geophysical Data Center, NOAA US Department of Commerce, Code E/GC3, Boulder, CO 80303

Foley JA, Kutzbach JE, Coe MT, Levis S (1994) Feedbacks between climate and boreal forests during the Holocene epoch. Nature 371 (6492): 52–54

Fouquart Y, Bonnel B (1980) Computations of solar heating of the earth's atmosphere: a new parametrization. Beitr Phys Atmos 53: 35–62

Gallée H, van Ypersele JP, Fichefet T, Tricot C, Berger A (1991) Simulation of the last glacial cycle by a coupled, sectorially averaged climate-ice sheet model. Part I: the climate model. J Geophys Res 96: 13,139–13,161

Ganopolski A, Kubatzki C, Claussen M, Brovkin V, Petoukhov V (1998) The influence of vegetation–atmosphere–ocean interaction on climate during the mid-Holocene. Science 280 (5371): 1916–1919

Gasse F (2000) Hydrological changes in the African tropics since the Last Glacial Maximum. Quat Sci Rev 19: 189–211

Gloersen P, Campbell WJ, Cavalieri DJ, Comiso JC, Parkinson CL, Zwally HJ (1992) Arctic and Antarctic sea ice, 1978–1987: satellite passive-microwave observations and analysis vol. SP-511 of Spec Publ NASA, Washington D.C., USA, pp 290

Goosse H, Fichefet T (2000) Open-ocean convection and polynya formation in a large-scale ice-ocean model. Tellus 53(1): 94–111

Hall NM, Valdes P (1997) An AGCM simulation of the climate 6000 years ago. J Clim 10: 3–17

Harrison SP, Jolly D, Laarif F, Abe-Ochi A, Dong B, Herterich K, Hewitt C, Joussaume S, Kutzbach JE, Mitchell J, d-e Noblet N, Valdes P (1998) Intercomparison of simulated global vegetation distributions in response to 6 kyr BP orbital forcing. J Clim 11(11): 2721–2742

Harvey LDD (1988) Development of a sea-ice model for use in zonally averaged energy balance models. J Clim 1: 1221–1238

Harvey LDD (1992) A two-dimensional ocean model for long-term climatic simulations: stability and coupling to atmospheric and sea-ice models. J Geophys Res 97: 9435–9453

Held IM, Hou AY (1980) Non-linear axially symmetric circulations in a nearly inviscid atmosphere. J Atmos Sci 37: 515–533

Hewitt C, Mitchell J (1998) A fully coupled GCM simulation of the climate of the mid-Holocene. Geophys Res Lett 25(3): 361–364

Hovine S, Fichefet T (1994) A zonally averaged, three-basin ocean circulation model for climate studies. Clim Dyn 10: 313–331

Hsiung J (1985) Estimates of global oceanic meridional heat transport. J Phys Oceanogr 15: 1405–1413

Hughes TJ, Denton GH, Anderson BG, Schiling DH, Fasthook JL, Linfle CS (1981) The last great ice sheets: a global view. In: Denton GH, Hughes TJ (eds) The last great ice sheets. Wiley Interscience Publications, USA, pp 275–317

Huntley B, Prentice IC (1988) July temperatures in Europe from pollen data, 6000 years before present. Science 241: 687–690

Indermühle A, Stocker TF, Joos F, Fisher H, Smith HJ, Wahlen M, Deck B, Mastroianni D, Tschumi J, Blunier T, Meyer R, Stauffer B (1999) Holocene carbon-cycle dynamics based on CO_2 trapped in ice at Taylor Dome, Antarctica. Nature 398: 121–126

Jaeger L (1976) Monatskarten des Nierderschlags für die ganze Erde Tech Rep 139 Ber Dtsch Wetterdienstes pp 38

Joussaume S, Braconnot P (1997) Sensitivity of paleoclimate simulation results to season definitions. J Geophys Res 102(D2): 1943–1956

Joussaume S et al. (1999) Monsoon changes for 6000 years ago: results of 18 simulations from the Paleoclimate Modeling Intercomparison Project (PMIP). Geophys Res Lett 26(7): 859–862

Kalnay E, Kanamitsu M, Kistler R, Collins W, Deaven D, Gandin L, Iredell M, Saha S, White G, Woollen J, Zhu Y, Leetmaa A, Reynolds R (1996) The NMC-NCAR 40 year reanalysis project. Bull Am Meteorol Soc 79: 789–799

Keith DW (1995) Meridional energy transport: uncertainty in zonal means. Tellus 47A: 30–44

Kerwin MW, Overpeck JT, Webb RS, de Vernal A, Rind DH, Healy RJ (1999) The role of oceanic forcing in mid-Holocene Northern Hemisphere climatic change. Paleoceanography 14(2): 200–210

Koç N, Jansen E, Haflidason H (1993) Paleoceanographic reconstructions of surface ocean conditions in the Greenland, Iceland and Norwegian Seas through the last 14 ka based on diatoms. Quat Sci Rev 12: 115–140

Koç N, Jansen E, Jald M, Labeyrie L (1996) Late glacial-Holocene sea surface temperatures and gradients between the North Atlantic and the Norwegian Sea: implications for the Nordic heat pump. In: Late Quaternary Palaoceanography of the North Atlantic Margins. Geological Society Special Publication 111, pp 177–185

Kubatzki C, Montoya M, Rahmstorf S, Ganopolski A, Claussen M (2000) Comparison of the last interglacial climate simulated by a coupled global model of intermediate complexity and an AOGCM. Clim Dyn 16: 799–814

Kutzbach JE, Liu Z (1997) Response of the African monsoon to orbital forcing and ocean feedbacks in the middle Holocene. Science 278: 440–443

Kutzbach JE, Otto-Bliesner BL (1982) The sensitivity of the African and Asian monsoon climate to orbital parameter changes for 9000 years BP in a low-resolution general circulation model. J Atmos Sci 39: 1177–1188

Kutzbach JE, Guetter PJ, Behling PJ, Selin R (1993) Simulated climatic changes: results of the COHMAP Climate-Model experiments. In: Wright HEJ, Kutzbach JE, Webb III T, Ruddiman WF, Street-Perrot FA, Bartlein PJ (eds) Global Climates since the Last Glacial Maximum. University of Minesota Press, USA, pp 24–92

Kutzbach JE, Bonan G, Foley J, Harrison SP (1996) Vegetation and soil feedbacks on the response of the African monsoon to orbital forcing in the early to middle Holocene. Nature 384: 623–626

Lambeck K, Yokoyama Y, Johnston P, Purcell A (2000) Global ice volumes at the Last Glacial Maximum and early Lateglacial. Earth Planet Sci Lett 181: 513–527

Levitus S (1982) Climatological Atlas of the World Ocean NOAA Prof. Pap 13 Nat Oceanic and Atmos Admin, US Department of Commerce Washington D.C., 173 pp

MacDonald GM, Velichko AA, Kremenetski CV, Borisova OK, Goleva AA, Andreev AA, Cwynar LC, Riding RT, Forman SL, Edwards TWD, Aravena R, Hammarlund D, Sziecz JM, Gattaulin VN (2000) Holocene treeline history and climate change across Northern Eurasia. Quat Res 53: 302–311

Morcrette JJ (1984) Sur la paramétrisation du rayonnement dans les modèles de la circulation générale atmosphérique. PhD Thesis Université des Sciences et Technologies de Lille, Lille, France, pp 373

Ohring G, Adler S (1978) Some experiments with a zonally-averaged climate model. J Atmos Sci 35: 186–205

Oort HH (1983) Global atmospheric circulation statistics 1958–1973 NOAA Prof Pap 14. Nat Oceanic and Atmos Admin, US Department of Commerce Washington DC, pp 180

Otto-Bliesner BL (1999) El niño/La Niña and Sahel precipitation during the middle Holocene. Geophys Res Lett 26(1): 87–90

Peltier W (1998) Postglacial variations in the level of the sea: implications for climate dynamics and solid-earth geophysics. Rev Geophys 36(4): 603–689

Peng L, Chou MD, Arking A (1987) Climate warming due to increasing atmospheric CO_2: simulations with a multilayer coupled atmosphere–ocean seasonal energy balance model. J Geophys Res 92: 5505–5521

Prather MC (1986) Numerical advection by conservation of second order moments. J Geophys Res 91(D6): 6671–6681

Prentice IC, Webb T (1998) Biome 6000: reconstructing global mid-Holocene vegetation patterns from palaeoecological records. J Biogeogr 25: 997–1005

Prentice IC, Cramer W, Harrison SP, Leemans R, Monserud RA, Solomon AM (1992) A global biome model based on plant physiology and dominance, soil properties and climate. J Biogeogr 19: 35–37

Ruddiman WF, Mix AC (1993) The North and Equatorial Atlantic at 9000 and 6000 yr BP. In: Wright HEJ, Kutzbach JE, Webb III T, Ruddiman WF, Street-Perrot F, Bartlein PJ (eds) Global climates since the Last Glacial Maximum. University of Minesota Press, USA pp 24–92

Saltzman B (1980) Parametrization of the vertical flux of latent heat at the Earth's surface for use in statistical-dynamical climate models. Arch Met Geophys Biokl A 29: 41–53

Saltzman B, Ashe S (1976) Parametrization of the monthly mean vertical heat transfer at the Earth's surface. Tellus 28: 323–331

Satoh M, Shiobora M, Takahashi M (1995) Hadley circulations and their rôles in the global angular momentum budget in two- and three-dimensional models. Tellus 47A: 548–560

Schmitz WJ (1995) On the interbasin-scale thermohaline circulation. Rev Geophys 33: 151–173

Sela J, Wiin-Nielsen A (1971) Simulation of the atmospheric annual energy cycle. Mon Weather Rev 99: 460–468

Sellers W (1983) A quasi-three-dimensional climate model. J Appl Meteorol 22: 1557–1574

Semtner AJ (1976) A model for the thermodynamic growth of sea ice in numerical investigations of climate. J Phys Oceanogr 6: 379–389

Semtner AJ (1986) Finite-difference formulation of a world ocean model. In: O'Brien JJ (ed) Advanced physical oceanographic numerical modelling. D. Reidel, Dordrecht, Netherlands, pp 187–202

Smith W (1966) Note on the relationship between total precipitable water and surface dew point. J Appl Meteorol 5: 726–727

Stein U, Alpert P (1993) Factor separation in numerical simulations. J Atmos Sci 50: 2107–2115

Street-Perrott FA, Mitchell J, Marchand D, Brunner J (1990) Milankovitch and albedo forcing of the tropical monsoons: a comparison of geological evidence and numerical simulations for 9000 yBP. Trans R Soc Edinburgh 81: 407–427

Taylor K (1976) The influence of subsurface energy storage on seasonal temperature variations. J Appl Meteorol 15: 1129–1138

TEMPO (1996) Potential role of vegetation feedback in the climate sensitivity of high-latitude regions: a case study at 6000 years BP. Global Biogeochem Cycles 10(4): 727–736

Texier D, de Noblet N, Harrison SP, Haxeltine A, Jolly D, Joussaume S, Laarif F, Prentice IC, Tarasov P (1997) Quantifying the role of biosphere–atmosphere feedbacks in climate change: coupled model simulations for 6000 years BP and comparison with paleodata for northern Eurasia and northern Africa. Clim Dyn 13: 865–882

Trenberth KE, Solomon A (1994) The global heat balance: heat transports in the atmosphere and ocean. Clim Dyn 10: 107–134

Vimeux F, Masson V, Jouzel J, Stievenard M, Petit JR (1999) Glacial-interglacial changes in ocean surface conditions in the southern hemisphere. Nature 398: 410–413

Vimeux F, Masson V, Jouzel J, Petit JR, Steig EJ, Stievenard M, Vaikmae R, White JWC (2001) Holocene hydrological cycle changes in the Southern Hemisphere documented in East Antarctic deuterium excess records. Clim Dyn 17(7): 503–513

Warren SG, Hahn CJ, London J, Chervin RM, Jenne RL (1986) Global distribution of total cloud cover and cloud type amounts over land. Technical note TN-273 + STR NCAR, Boulder, CO, USA, 29 pp + 200 maps

Woordward FI (1987) Climate and plant distribution. Cambridge University Press, New York, pp 174

Wright DG, Stocker TF (1992) Sensitivities of a zonally averaged global ocean circulation model. J Geophys Res 97: 12,707–12,730